

JGR Solid Earth

RESEARCH ARTICLE

10.1029/2020JB019683



Key Points:

- New constitutive model for (de) compaction of porous viscoelastoplastic rocks in the presence of shear is proposed
- Model accounts for shear-enhanced compaction, shear-induced dilation, and material nonlinearity in agreement with experimental data
- New analytical and numerical solutions show that chimney-like porosity waves can be generated at fluid pressure below the lithostatic stress

Correspondence to:

V. M. Yarushina,
viktoriya.yarushina@ife.no

Citation:

Yarushina, V. M., Podladchikov, Y. Y., & Wang, L. H. (2020). Model for (de) compaction and porosity waves in porous rocks under shear stresses. *Journal of Geophysical Research: Solid Earth*, 125, e2020JB019683. <https://doi.org/10.1029/2020JB019683>

Received 28 FEB 2020

Accepted 1 JUL 2020

Accepted article online 11 JUL 2020

Model for (De)Compaction and Porosity Waves in Porous Rocks Under Shear Stresses

V. M. Yarushina¹ , Y. Y. Podladchikov^{2,3} , and L. H. Wang¹ 

¹Institute for Energy Technology, Kjeller, Norway, ²Institut des Sciences de la Terre, University of Lausanne, Lausanne, Switzerland, ³Faculty of Mechanics and Mathematics, Moscow State University, Moscow, Russia

Abstract An understanding of instantaneous and long-term compaction of porous rocks is important for reservoir engineering and Earth sciences. Experience from laboratory triaxial compression tests and from subsurface operations indicates that shear and volumetric deformations are interdependent. Their mutual dependence results in shear-enhanced compaction and shear-induced dilation under short-term and long-term loading. Using a classical averaging approach, we consider the evolution of a single fluid-filled pore in a solid elastoplastic or viscoplastic matrix under combined pressure and shear loading to introduce a new failure envelope and 3-D constitutive relations for both rate-dependent and rate-independent deformation of porous rocks. Our model provides a simple description of rock behavior under a wide range of strain rates. The model predictions agree well with experimental data from triaxial instantaneous and creep tests. Analytical and numerical solutions for solitary porosity wave propagation in viscoplastic rocks in the presence of shear were obtained. New solutions show that new rheological laws have serious implications for porosity waves. Plasticity onset leads to compaction-decompaction asymmetry and the formation of elongated channel-like porosity waves. Shear-induced dilation facilitates porosity wave propagation at fluid pressures below the lithostatic stress. This makes porosity waves a viable mechanism in the formation of focused fluid flow structures in crustal rocks.

1. Introduction

Many engineering and natural processes in the Earth involve coupled rock deformation and fluid flow (Cai & Bercovici, 2013; Connolly & Podladchikov, 2015; Keller et al., 2013; Petrini et al., 2020; Yarushina et al., 2013). Models describing fluid flow in deformable porous rocks can be based in part on the principles of irreversible thermodynamics (Yarushina & Podladchikov, 2015). Still, the formulation of closure relations represents a significant challenge. The compaction relation that describes volumetric deformation and porosity evolution during external loading is particularly important because it directly affects fluid flow. The combination of irreversible thermodynamics and microscale physics places some constraints on the form of compaction relation (Yarushina & Podladchikov, 2015). It is well known that the short-term response of most of the compacting porous rocks is elastoplastic (Fortin et al., 2007; Guéguen et al., 2004; Labuz et al., 2018; Makhnenco & Labuz, 2016), while, on a longer time scale, rocks also exhibit viscous properties (Brantut et al., 2013; Chang & Zoback, 2009; Hangx et al., 2010; Makhnenco & Podladchikov, 2018; Renner et al., 2001; Sabitova et al., 2019). Viscous deformation affects the performance of petroleum reservoirs, leading to wellbore stability issues, fault reactivation, and seafloor subsidence (Maranini & Brignoli, 1999). In geotechnical engineering, viscous deformation affects the stability of rock slopes and underground structures, such as tunnels and nuclear waste repositories (Fabre & Pellet, 2006; Ghanbarzadeh et al., 2015; Ma & Daemen, 2006; Tsai et al., 2008). Constitutive models that represent the rate-dependent stress-strain response are implemented in the commercial software (Crook et al., 2008) and are used in numerical studies of reservoir depletion, subsidence, and associated microseismicity (Angus et al., 2015; Yarushina et al., 2017). Viscous deformation and strong coupling between fluid flow and geomechanical deformation can eventually lead to the formation of focused fluid flow, often evidenced in the Earth as dikes, veins, volcanic diatremes, or seismic chimneys (Räss et al., 2014; Yarushina, Podladchikov, et al., 2015; Minakov et al., 2017). Seismic chimneys are of particular economic importance, as their presence was repeatedly identified as being the most likely indication of leakage and expulsion of gas, oil, and, possibly, CO₂.

Classical theories of poroelasticity and poroviscosity as formulated by Biot (1962) and McKenzie (1984) treat shear deformation and compaction as two independent processes. During shear deformation, stress deviator

©2020. The Authors.

This is an open access article under the terms of the Creative Commons Attribution License, which permits use, distribution and reproduction in any medium, provided the original work is properly cited.

is related to deviatoric strain or strain rate, while compaction is fully described by the linear relationship between effective pressure and volumetric strain or strain rate. However, experimental evidence suggests that shear deformation in rocks is strongly coupled with volumetric deformation, leading to such phenomena as shear-induced dilation at low confining pressures and shear-enhanced compaction at higher confining pressures (Baud et al., 2006; Fortin et al., 2006; Kohlstedt & Holtzman, 2009; Tsai et al., 2008; Xiao & Evans, 2003; Zhu et al., 1997). Shear-enhanced compaction and shear-induced dilation occur both in the upper crustal conditions where elastoplastic deformation of the rock prevails and in viscously deforming partially molten rocks representing Earth's mantle.

Shear-enhanced compaction has important consequences for engineering practice, as observed during the depletion of reservoirs (Chin et al., 1993), when pore pressure reduction leads to a nonisotropic change in stresses. Shear-enhanced compaction induces considerable permeability and porosity reduction, thus affecting fluid flow (Xiao et al., 2006; Zhu et al., 1997). It is especially pronounced in weak rocks, which are prone to creep, resulting in many engineering problems such as underestimated subsidence and loss of stability of underground constructions (Tsai et al., 2008). There is field evidence of shear-enhanced compaction bands formed in nature due to the interplay between shear and volumetric deformation in the crust (Eichhubl et al., 2010; Fossen et al., 2011). In general, shear-enhanced compaction might be important for geological settings where shear and compaction act simultaneously, for example, at mid-ocean ridges where mantle upwelling due to buoyancy is influenced by the mantle shear caused by spreading oceanic plates (Connolly & Podladchikov, 2007; Spiegelman & Mckenzie, 1987) and subduction zones (Gerya & Yuen, 2003). The process of shear-enhanced compaction is very tightly linked to strain localization. In the mantle, this leads to the formation of melt-enriched shear zones, which may significantly contribute to melt extraction by forming high-permeability fluid pathways (Katz et al., 2006; Kohlstedt & Holtzman, 2009; Rudge & Bercovici, 2015; Spiegelman, 2003). In the crust, the transition from shear-enhanced compaction to brittle faulting leads to the generation of earthquakes (Regenauer-Lieb & Yuen, 2003). Enhanced compaction in the presence of shear is usually attributed to plastic deformation. Elastoplastic models from rock mechanics (Rudnicki & Rice, 1975) or critical state models from soil mechanics (Schofield & Wroth, 1968) are usually used to describe shear-enhanced compaction. In viscous rocks, shear localization with dilation and shear-enhanced compaction were previously attributed to damage and were accounted for in the two-phase damage models (Lyakhovsky et al., 2015; Ricard & Bercovici, 2003). However, there is no current model that accounts for the effect of shear stresses on bulk viscoelastoplastic deformation of porous rocks and porous flow. This paper is an attempt to fill this gap.

Recently, Yarushina and Podladchikov (2015) formulated constitutive relations for porous viscoelastoplastic rocks. While conservation equations were derived based on the principles of irreversible thermodynamics, closure relations were obtained based on the effective media theory by looking at the effective behavior of rocks containing idealized cylindrical or spherical pores. This theory was limited to hydrostatic compaction and decompression. It was shown that in the linearly elastic limit, the model reproduced well-known Biot's equations (Biot, 1941), while in the viscous limit, it was consistent with popular models for porous flow in magma (e.g., Mckenzie, 1984; Stevenson & Scott, 1991). This model was implemented into several numerical codes and was applied to studies of fluid flow focusing (Omlin et al., 2018). Now, we elaborate on this model further by including the effects of shear stresses on (de)compaction processes and, thus, on fluid flow. We derive new analytical solutions or use classical ones, if available, to predict the mechanical response of the representative volume element (RVE) to mechanical load. Using a simple averaging procedure, we derive closure relations for elastic, plastic, and viscoplastic deformation. The resulting equations are formulated in the form which resembles classical elastoplastic flow theories so that numerical implementation of the new equations would be straightforward. The influence of shear stresses on fluid flow is studied based on the geological system with propagating porosity waves.

2. Micromechanical Model

Yield surface is a central notion in the plasticity theory. Its shape distinguishes the plasticity of metals from the plasticity of rocks. However, elastoplastic models largely remain phenomenological and postulate a specific form of the yield surface. Attempts to obtain the yield surface and stress-strain relations based on microscale physics remain limited. Existing models are based mainly on purely elastic solutions in which the first

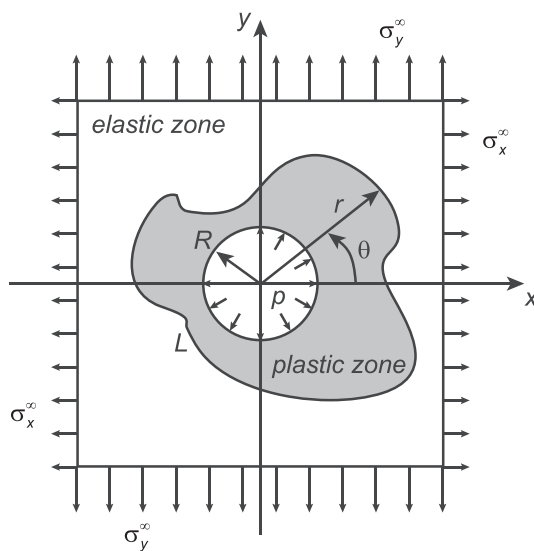


Figure 1. Schematic of a representative volume element for porous rock. An infinite body of incompressible elastoplastic (viscoplastic) material containing a long cylindrical pore with radius R is subject to a uniform remote stress $\sigma_x^\infty \neq \sigma_y^\infty$, $\sigma_{xy}^\infty = 0$. A uniform pressure p is applied at the pore boundary in fluid-saturated porous material. In dry rocks, the pore boundary is traction-free.

occurrence of critical stress is marked as plasticity onset and the manifold of such yield points is considered a yield surface (Curran & Carroll, 1979; Sevostianov & Kachanov, 2001). Other attempts postulate a specific simplified form of the yield surface and then use ideally plastic solutions to constrain the material parameters used in these laws (Green, 1972). Thus, the evolution of the yield surface during loading, that is, hardening or softening behavior and complete stress-strain relation, cannot be captured by such models. Stress-strain, or compaction, relations are usually fitted using complicated hardening laws involving a number of fitting parameters (Carroll, 1991). The approximate relation between the growth rate of an isolated void and imposed nonhydrostatic stress and strain was developed for simplistic cases of rigid-perfectly plastic materials (Gurson, 1977; Rice & Tracey, 1969) and nonlinear viscous materials (Budiansky et al., 1982). These models are based on the simple problem of the growth (contraction) of an isolated spherical or cylindrical void in an infinite solid matrix. Duva and Hutchinson (1984) use a similar spherical model with approximate solutions to obtain complete stress-strain relations for nonlinearly viscous materials. A viscous damage theory for porous low-cohesion rocks was derived by Ricard and Bercovici (2003), who considered matrix containing isolated voids. This model provides the complete stress-strain relation and predicts enhanced compaction rates in the presence of shear. Triaxial deformation of elastic-viscoplastic porous solid was numerically studied by Koplik and Needleman (1988) on an array of spherical voids. Their results reflect faster compaction rates in the presence of shear.

In this paper, constitutive equations are derived for an incompressible isotropic matrix material containing a dilute distribution of elongated cylindrical pores. The short- and long-term behavior of porous rock is accounted for by considering both rate-independent elastoplastic and rate-dependent viscoplastic deformation. Our RVE consists of a single cylindrical pore subject to spatially homogeneous fluid pressure and non-hydrostatic far-field stresses representing plane strain loading conditions (Figure 1). We explicitly account for elastoplastic (viscoplastic) deformation of a single pore and its shape evolution during deformation. As this is an already complicated problem, we choose the simplest dilute distribution averaging scheme. This scheme ignores the interaction between the pores and, thus, might be inaccurate at high porosities. However, we show that our model accurately reproduces published experimental data. In the elastoplastic regime, deformation and stresses around the pore can be described using the classical analytical solution of Galin (1946). For the viscoplastic regime, we derived a new analytical solution by modifying elastic and elastoplastic solutions using the viscoelastic correspondence principle. We assume that the initial yield of the matrix material on the microscale is determined by the von Mises criterion. The interested reader can find analytical solutions for the stress and strain fields in the representative volume in Appendix A. Averaging of the analytical solution provides the relation between volumetric strain and stresses for elastic, elastoplastic, and viscoplastic regimes (see Appendix B for complete derivations). The obtained macroscopic compaction relations can be rewritten in a form compatible with the plastic flow theory and, thus, can be further used to derive the functional form of the failure envelope. Because we consider both contraction and dilation of the pores, our solution provides a complete failure envelope that accounts for tensile, shear, and compaction failure.

3. Macroscale Constitutive Equations for Porous Rocks

Classical viscous models in geodynamics assume that viscous deformation is accumulated in response to any stress over time. The stress-strain rate behavior remains the same for high and low stresses (Gerya, 2019; McKenzie, 1984; Stevenson & Scott, 1991). On the other hand, existing viscoplastic models that were applied largely to metals assume that viscoplastic flow occurs only when stresses reach yield stress (Chaboche, 2008; Perzyna, 1966; Perzyna & Drabik, 1989). Laboratory experiments show that viscous deformation can be accumulated even at low stresses and that stress-strain rate behavior changes at higher stress levels

Table 1
List of Principal Notations

Symbol	Meaning
C	Pore geometry factor
$F = F(p_e, \tau, \varepsilon^P)$	Yield function
G, G_d	Shear modulus of intact rock, drained shear modulus of porous rock
g	Gravitational constant
h	Linear hardening parameter
K_d	Drained bulk modulus of porous rock
m	Pressure exponent in the yield function
n	Shear stress exponent in the yield function
p_e, \bar{p}, p_f, p_c	Effective, total, fluid, and confining pressures
$Q = Q(p_e, \tau)$	Plastic flow potential
T	Time
$W = W(p_e, \tau)$	Viscoplastic flow potential
Y	Reference yield stresses in the yield function
α	Ratio of shear and bulk viscosities in porosity wave solution
α_τ	Effective pressure coefficient in the yield function
γ_{ij}	Deviatoric components of total strain
ε	Volumetric component of total strain
η_b, η_s	Bulk and shear viscosities of porous viscous rock, effective bulk viscosity of viscoplastic rock
η_{eff}, η_{shear}	Effective bulk and shear viscosities of viscoplastic rocks
κ, κ_b	Permeability and constant background permeability in solitary wave
λ, Λ	Plastic and viscoplastic multipliers
μ	Fluid shear viscosity
ν	Permeability exponent
$\bar{\rho}, \rho_f, \rho_s$	Bulk, fluid, and solid densities
σ_i	Principal components of stress tensor
τ, τ_0	Equivalent shear stress, critical shear stress in the yield function
τ_{ij}	Components of total stress deviator
φ, φ_b	Porosity, constant background porosity in porosity wave
ω	Nondimensional speed of porosity wave

(Maranini & Brignoli, 1999; Sabitova et al., 2019; Tsai et al., 2008). Viscous and viscoplastic constitutive equations admit stresses within, on, and outside the yield surface. Plastic constitutive laws admit stresses only within and on the yield surface, which limits the unrealistic stress buildup possible in viscous models. Thus, to keep classical limits and be consistent with experimental observations, we assume that the total strain rates $\dot{\varepsilon}_{ij}$ can be split into elastic (i.e., reversible), plastic (i.e., time-independent and irreversible), viscous, and viscoplastic (i.e., time-dependent and irreversible) parts as follows:

$$\dot{\varepsilon}_{ij} = \dot{\varepsilon}_{ij}^e + \dot{\varepsilon}_{ij}^p + \dot{\varepsilon}_{ij}^v + \dot{\varepsilon}_{ij}^{vp}. \quad (1)$$

Thus, the total inelastic deformation is a sum of instantaneous plastic strain and accumulated viscoelastic and viscoplastic strain, reflecting the evolution of the microstructure. Viscoplastic deformation is independent of the loading history and is a function of the current stress state only, while plastic strains depend on the loading history. Volume averaging procedures show that in homogeneous isotropic rocks, elastic volumetric deformation is unaffected by shear stresses (Appendix B, see also Yarushina, Räss, et al., 2015). Thus, the usual incremental poroelastic constitutive equations that are fully consistent with Biot's theory can be used for $\dot{\varepsilon}_{ij}^e$:

$$\dot{\bar{p}} - \alpha_{BW} \dot{p}_f = K_d \dot{\varepsilon}^e, \quad \dot{\tau}_{ij} = 2G_d \dot{\gamma}_{ij}^e \quad (2)$$

where $\bar{p} = \varphi p_f + (1 - \varphi)p_s$ is the total pressure, p_f, p_s are fluid and solid pressures, φ is the porosity, τ_{ij} is the total stress deviator, $\dot{\varepsilon}^e$ is the volumetric elastic strain rate, $\dot{\gamma}_{ij}^e$ is the deviatoric elastic strain rate, α_{BW} is the Biot-Willis coefficient, K_d is the drained bulk modulus, and G_d is the drained shear modulus, while dot denotes the material time derivative (see Table 1 for notations). Positive sign of strain indicates compression. These equations were derived multiple times based on principles of irreversible thermodynamics and effective media theory (e.g., Coussy, 2004; Lopatnikov & Cheng, 2004; Yarushina & Podladchikov, 2015, and references therein). Plastic constitutive equations can be written using the nonassociated flow rule:

$$\dot{\varepsilon}^p = \dot{\lambda} \frac{\partial Q}{\partial p_e}, \quad \dot{\gamma}_{ij}^p = \dot{\lambda} \frac{\partial Q}{\partial \tau_{ij}} \quad (3)$$

where $Q = Q(p_e, \tau_{ij})$ is the plastic potential, $\dot{\lambda}$ is the nonnegative plastic multiplier, and $p_e = \bar{p} - p_f$ is the effective pressure. The plastic flow rule must be accompanied by the yield criterion and standard plastic consistency conditions, which together limit stress buildup.

Viscous strain rates do not require threshold stress and are linearly related to stresses (e.g., Yarushina & Podladchikov, 2015, and references therein), namely,

$$\dot{\varepsilon}^v = \frac{p_e}{\eta_b}, \quad \dot{\gamma}_{ij}^v = \frac{\tau_{ij}}{2\eta_s} \quad (4)$$

where η_b and η_s are the bulk and shear viscosities, which, among other things, might depend on temperature and porosity. Our micromechanical model suggests that the simplest porosity dependence has the form

$$\eta_b = C\eta_s(1 - \varphi)/\varphi \quad (5)$$

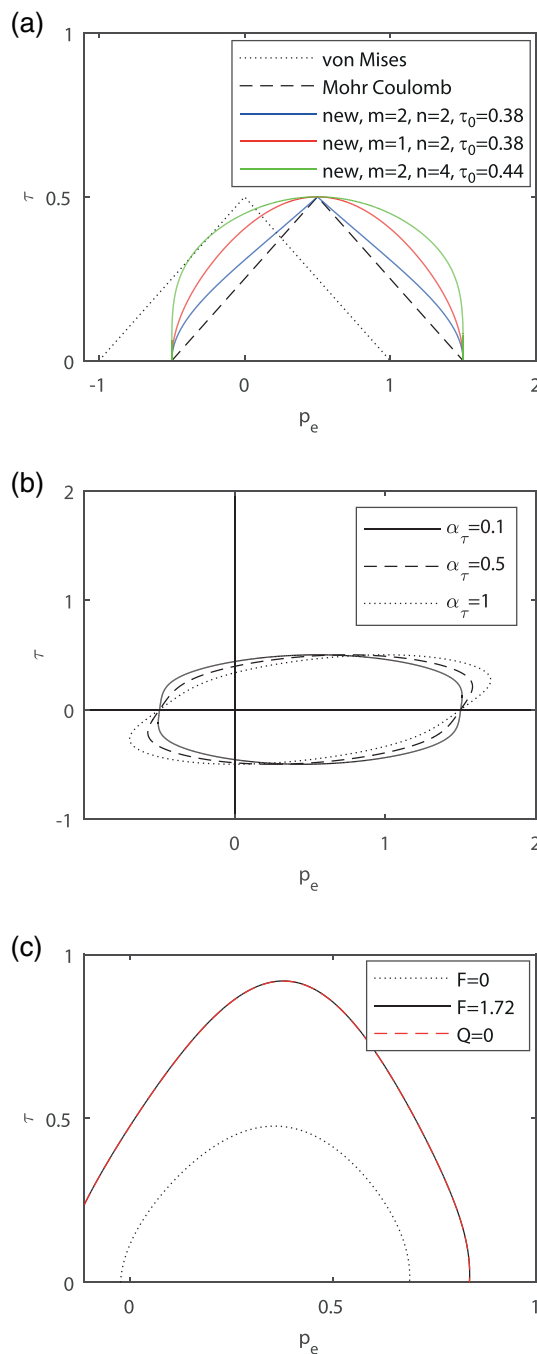


Figure 2. (a) Shape of the new proposed yield surface given by Equation 8 at different values of parameters n and m ($Y = 1, p_0 = 0.5, \alpha_\tau = 0$) compared to the theoretical plasticity onset around a cylindrical void in a solid matrix obeying von Mises and Mohr-Coulomb yield criteria. (b) Shape of the new yield surface at different values of α_τ ($Y = 1, p_0 = 0.5, m = 2, n = 4, \tau_0 = 0.44$). (c) Shape of the viscoplastic potential versus yield surface.

where C is the geometrical factor, which is equal to 1 for cylindrical pores, $4/3$ for spheres, and $\ll 1$ for elliptical or crack-like pores (Bercovici et al., 2001; Schmeling, 2000; Yarushina & Podladchikov, 2015). Often, viscoplastic strain rates are described by means of a viscoplastic flow rule (Chaboche, 2008; Heeres et al., 2002; Perzyna, 1966; Perzyna & Drabik, 1989). Our micromechanical model results in the following simplest viscoplastic flow rule:

$$\dot{\epsilon}^{vp} = \Lambda \begin{cases} 0 & \text{if } F(p_e, \tau_{ij}, \dot{\epsilon}^p) < 0 \\ \frac{\partial W}{\partial p_e} & \text{if } F(p_e, \tau_{ij}, \dot{\epsilon}^p) \geq 0 \end{cases} \quad (6)$$

$$\dot{\gamma}_{ij}^{vp} = \Lambda \begin{cases} 0 & \text{if } F(p_e, \tau_{ij}, \dot{\epsilon}^p) < 0 \\ \frac{\partial W}{\partial \tau_{ij}} & \text{if } F(p_e, \tau_{ij}, \dot{\epsilon}^p) \geq 0 \end{cases} \quad (7)$$

where Y is the yield stress and W is the viscoplastic potential that will be defined in the next section. The gradient of W determines the direction of viscoplastic flow. A nonnegative viscosity consistency parameter $\Lambda \geq 0$ specifies the magnitude of viscoplastic strain rates. Its values must be calibrated experimentally.

3.1. Yield Criterion

In porous rocks, the yield criterion is a somewhat arbitrary notion, as it might correspond to the onset of local plastic failure around stress concentrators (such as in the models of Curran & Carroll, 1979 and Sevostianov & Kachanov, 2001), or it might correspond to the point where plasticity is significant and plastic zones around individual imperfections have coalesced (e.g., Green, 1972). In our geometrically simple model, plasticity onset around individual cylindrical pores in a matrix obeying the von Mises or Tresca yield criterion will be defined by the rhomb centered around point $p_e = 0, \tau = 0$ (black dotted line in Figure 2a). If smaller imperfections are present, as in dual porosity materials, the matrix will obey the Mohr-Coulomb yield criterion, and plasticity onset around a single pore will be determined by the same rhomb shifted along p_e axis by $p_0 = C_0 \tan \phi$, where C_0 is cohesion and ϕ is the angle of internal friction of the matrix material (black dashed triangle in Figure 2a). However, plasticity onset around an individual pore is not representative of the macroscopic yield condition. Yield onset around individual pores first results in a nonlinear deformation. Macroscopic plastic flow occurs when growing plastic zones around individual pores start to significantly influence the stress-strain response of the rock. This is illustrated in triaxial compaction experiments, where rock failure is monitored by acoustic emission. Indeed, acoustic emission starts much earlier than macroscopic failure of the sample exhibits itself by deflection of a compaction curve (Fortin et al., 2006, 2009; Stanchits et al., 2011). Such deflection is accompanied by a significant increase in acoustic emission. Thus, the shape of the compaction curve provides important indications of the plasticity onset. Let us note that yield function enters into elastoplastic stress-strain relations

after the plastic flow rule 3 is complemented with the standard plastic consistency condition (e.g., Chakrabarty, 1987; Yarushina et al., 2010; Gerbault et al., 1998) (see Equation B17 in Appendix B). Therefore, yield function can be obtained by integrating the theoretical elastoplastic compaction equation. The theoretical compaction equation is derived by averaging the analytical solution for deformation of the

pore in a nonhydrostatic stress field (see Appendix B for derivations). The resulting yield function takes the form

$$F = \left(1 + \left(\frac{\tau}{\tau_0}\right)^n\right) \exp\left(\left|\frac{p_e - \alpha_\tau \tau - p_0}{Y}\right|^m - 1\right) Y - Y - \frac{h}{\varphi} \varepsilon^p \quad (8)$$

where $\tau = \sqrt{\frac{3}{2}\tau_{ij}\tau_{ij}}$ is the equivalent shear stress. The shape of the corresponding failure envelope is characterized by six independent material parameters: n , m , τ_0 , Y , p_0 , and α_τ (Figures 2a and 2b). Linear hardening modulus h defines the evolution of the yield surface, which corresponds to the isotropic expansion of the initial yield surface. Parameters Y and p_0 define tensile and compaction strength. The tensile failure limit is defined by the critical stress $Y_d = p_0 - Y$, while critical pressure for the onset of pore collapse is given by $Y_c = p_0 + Y$. Usually, in experiments, this pressure corresponds to the upsurge in the acoustic emission activity (e.g., Fortin et al., 2009). Because pores and imperfections are present on all scales, decompaction strength in geological materials is different from pore collapse pressure. In the absence of imperfections of smaller size, for example, in porous metals, the failure envelope would be symmetrical with respect to the τ and p axes and $\alpha_\tau = 0$, $p_0 = 0$. Exponents n and m define the curvature of the failure envelope. These depend on the pore geometry and their interaction. In the material with very low porosity composed of aligned cylindrical pores, $n = 2$, $m = 1$, and $\tau_0 = Y/\sqrt{5}$. The failure envelope for these values of parameters is shown as a blue line in Figure 2a. Deviations from idealized geometry lead to different values of these parameters and, thus, to different shapes of the failure envelope. Parameter α_τ defines the asymmetry of the failure envelope with respect to the p axis (Figure 2b), that is, different plastic moduli in extension and compaction triaxial tests. Note that the derived failure surface encircles rhombs describing failure onset around individual pores.

3.2. Viscoplastic Flow Potential

Viscoplastic flow potential may depend on the yield function, $W = W(F)$. In this case, the viscoplastic flow rule is associative and viscoplastic flow is normal to the yield surface. For nonassociative viscoplasticity, W might depend on some other stress function. Here, viscoplastic flow potential W was chosen in a form that both reproduces the theoretical compaction relation derived from the micromechanical model and reduces to zero at the yield surface. The latter requirement guarantees the continuity of strain rates with failure onset. We suggest the following functional form of the viscoplastic potential:

$$W = (f - Y) \exp(f/Y) \quad (9)$$

where

$$f = Y \ln\left(\frac{F}{Y} + 1\right) = Y \ln\left(1 + \left(\frac{\tau}{\tau_0}\right)^n\right) + Y \left(\left|\frac{p_e - \alpha_\tau \tau - p_0}{Y}\right|^m - 1\right) \quad (10)$$

Function f is obtained by taking the logarithm of $F/Y+1$ when hardening is ignored. Thus, it represents an alternative form of the yield function. One can see that $f = 0$ when $F = 0$. The shape of surface $W = 0$ is quite like failure envelopes (Figure 2c). Substitution of Equations 9 and 10 results in the following associated viscoplastic flow rule.

$$\dot{\varepsilon}^{vp} = \Lambda \begin{cases} 0 & \text{if } F(p_e, \tau_{ij}, \varepsilon^p) < 0 \\ \frac{f}{Y} \exp\left(\frac{f}{Y}\right) \frac{\partial f}{\partial p_e} & \text{if } F(p_e, \tau_{ij}, \varepsilon^p) \geq 0 \end{cases} \quad (11)$$

$$\dot{\gamma}_{ij}^{vp} = \Lambda \begin{cases} 0 & \text{if } F(p_e, \tau_{ij}, \varepsilon^p) < 0 \\ \frac{f}{Y} \exp\left(\frac{f}{Y}\right) \frac{\partial f}{\partial \tau_{ij}} & \text{if } F(p_e, \tau_{ij}, \varepsilon^p) \geq 0 \end{cases} \quad (12)$$

where

$$\frac{\partial f}{\partial p_e} = m \left| \frac{p_e - \alpha_\tau \tau - p_0}{Y} \right|^{m-1} \operatorname{sgn}(p_e - \alpha_\tau \tau - p_0) \quad (13)$$

$$\frac{\partial f}{\partial \tau} = \frac{nY}{\tau_0} \left(\frac{\tau}{\tau_0} \right)^{n-1} \left(1 + \left(\frac{\tau}{\tau_0} \right)^n \right)^{-1} - \alpha_\tau m \left| \frac{p_e - \alpha_\tau \tau - p_0}{Y} \right|^{m-1} \operatorname{sgn}(p_e - \alpha_\tau \tau - p_0) \quad (14)$$

To avoid singularities that lead to numerical issues, we suggest using even values of m . In the simplest case of $m = 2$ and $\alpha_\tau = 0$

$$\frac{\partial f}{\partial p_e} = 2 \frac{p_e - p_0}{Y}, \quad \frac{\partial f}{\partial \tau} = \frac{nY}{\tau_0} \left(\frac{\tau}{\tau_0} \right)^{n-1} \left(1 + \left(\frac{\tau}{\tau_0} \right)^n \right)^{-1} \quad (15)$$

Combining viscous and viscoplastic strain rates, we obtain the following total rate-dependent, or creep, part of deformation, $\dot{\varepsilon}^c = \dot{\varepsilon}^v + \dot{\varepsilon}^{vp}$, $\dot{\gamma}_{ij}^c = \dot{\gamma}_{ij}^v + \dot{\gamma}_{ij}^{vp}$:

$$\dot{\varepsilon}^c = \frac{1}{\eta_b} \begin{cases} p_e & \text{if } F(p_e, \tau_{ij}, \varepsilon^p) < 0 \\ \Lambda \eta_b \frac{f}{Y} \exp\left(\frac{f}{Y}\right) \frac{\partial f}{\partial p_e} + p_e & \text{if } F(p_e, \tau_{ij}, \varepsilon^p) \geq 0 \end{cases} \quad (16)$$

$$\dot{\gamma}_{ij}^c = \frac{1}{2\eta_s} \begin{cases} \tau_{ij} & \text{if } F(p_e, \tau_{ij}, \varepsilon^p) < 0 \\ 2\Lambda \eta_s \frac{f}{Y} \exp\left(\frac{f}{Y}\right) \frac{\partial f}{\partial \tau} \frac{\partial \tau}{\partial \tau_{ij}} + \tau_{ij} & \text{if } F(p_e, \tau_{ij}, \varepsilon^p) \geq 0 \end{cases} \quad (17)$$

For the simplest case of $m = 2$ and $\alpha_\tau = 0$

$$\dot{\varepsilon}^c = \frac{1}{\eta_b} \begin{cases} p_e & \text{if } F(p_e, \tau_{ij}, \varepsilon^p) < 0 \\ \left(2 \frac{\Lambda \eta_b}{Y^2} f \exp\left(\frac{f}{Y}\right) + 1 \right) p_e - 2 \Lambda f \exp\left(\frac{f}{Y}\right) \frac{\eta_b p_0}{Y^2} & \text{if } F(p_e, \tau_{ij}, \varepsilon^p) \geq 0 \end{cases} \quad (18)$$

$$\dot{\gamma}_{ij}^c = \frac{\tau_{ij}}{2\eta_s} \begin{cases} 1 & \text{if } F(p_e, \tau_{ij}, \varepsilon^p) < 0 \\ \left(2 \frac{\Lambda \eta_s}{2\tau_0^2} f \exp\left(\frac{f}{Y}\right) \left(\frac{\tau}{\tau_0} \right)^{n-2} \left(1 + \left(\frac{\tau}{\tau_0} \right)^n \right)^{-1} + 1 \right) & \text{if } F(p_e, \tau_{ij}, \varepsilon^p) \geq 0 \end{cases} \quad (19)$$

These equations are rewritten in a simpler form

$$\dot{\varepsilon}^c = \frac{p_e - p_d}{\eta_{eff}}, \quad (20)$$

$$\dot{\gamma}_{ij}^c = \frac{\tau_{ij}}{2\eta_{shear}}, \quad (21)$$

that is reminiscent of previous viscous equations used in many analytical and numerical models (Connolly & Podladchikov, 2007; Gerya, 2019; Omlin et al., 2018; Schmeling et al., 2012; Yarushina, Podladchikov, et al., 2015). Here,

$$\eta_{eff} = \eta_b \begin{cases} 1 & \text{if } F(p_e, \tau_{ij}, \varepsilon^p) < 0 \\ \left(2 \frac{\Lambda \eta_b}{Y^2} f \exp\left(\frac{f}{Y}\right) + 1 \right)^{-1} & \text{if } F(p_e, \tau_{ij}, \varepsilon^p) \geq 0 \end{cases} \quad (22)$$

is the effective total bulk viscosity of visco-viscoplastic rocks,

$$p_d = \begin{cases} 0 & \text{if } F(p_e, \tau_{ij}, \varepsilon^p) < 0 \\ 2 \Lambda \frac{p_0 \eta_b}{Y^2} f \exp\left(\frac{f}{Y}\right) \left(2 \eta_b \frac{\Lambda f}{Y^2} \exp\left(\frac{f}{Y}\right) + 1 \right)^{-1} & \text{if } F(p_e, \tau_{ij}, \varepsilon^p) \geq 0 \end{cases} \quad (23)$$

is the dilation pressure, and

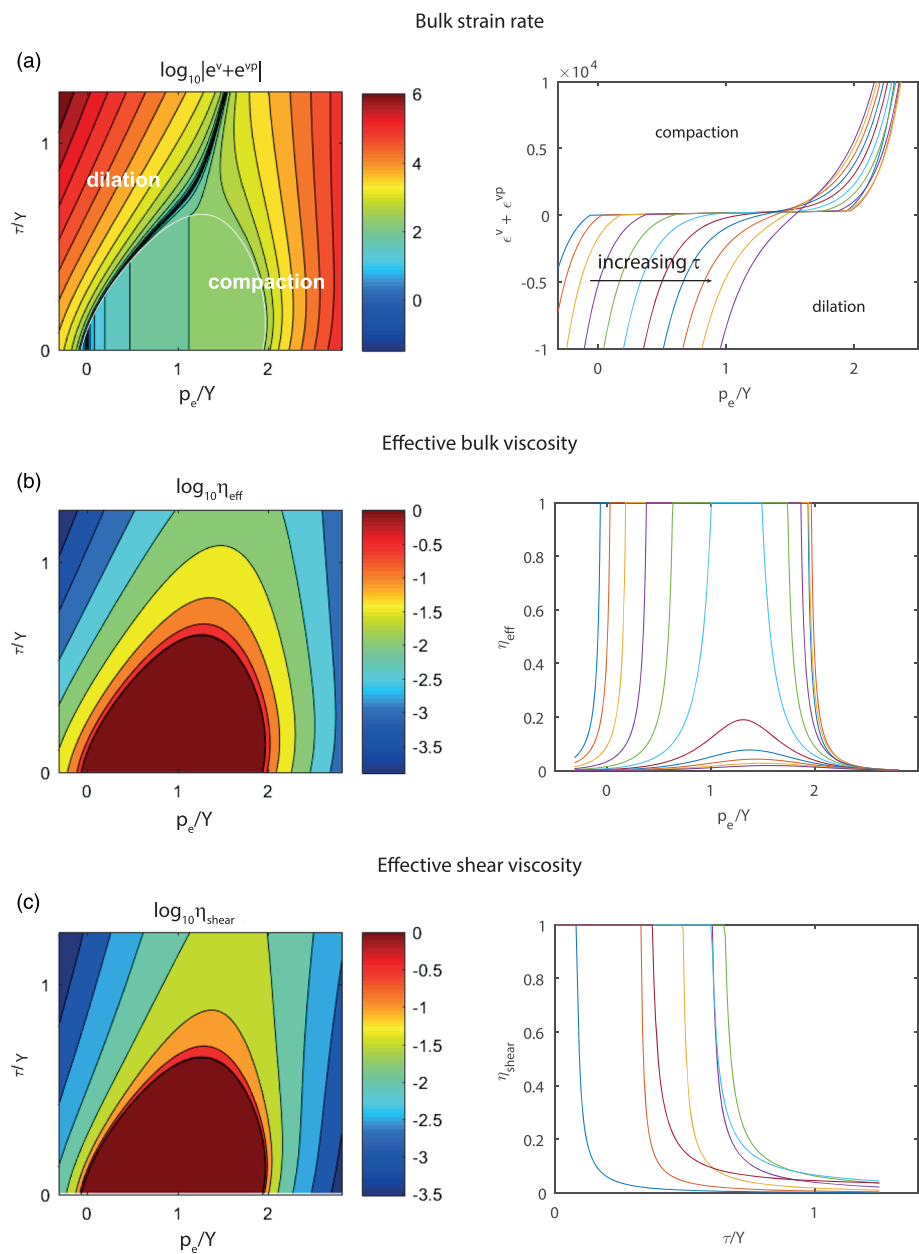


Figure 3. Theoretical predictions for rate-dependent deformation. (a) Dependence of bulk strain rate $\dot{\epsilon}^v + \dot{\epsilon}^{vp}$ on effective pressure and effective shear stress. The solid white line on the left figure shows the failure envelope, while the thick black line represents the compaction/dilation boundary. Dilation is possible at compressive effective pressures ($p_e > 0$). Plasticity onset significantly enhances the strain rate. Colored lines on the right figure correspond to different values of shear stress. (b) Effective bulk viscosity as a function of effective pressure and shear stress. Effective bulk viscosity reduces with plasticity onset, with both increasing and decreasing effective pressures. (c) Effective shear viscosity as a function of effective pressure and shear stress.

$$\eta_{shear} = \eta_s \begin{cases} 1 & \text{if } F(p_e, \tau_{ij}, \dot{\epsilon}^p) < 0 \\ \left[\Lambda \frac{3n\eta_s f}{2\tau_0^2} \exp\left(\frac{f}{Y}\right) \left(\frac{\tau}{\tau_0}\right)^{n-2} \left(1 + \left(\frac{\tau}{\tau_0}\right)^n\right)^{-1} + 1 \right]^{-1} & \text{if } F(p_e, \tau_{ij}, \dot{\epsilon}^p) \geq 0 \end{cases} \quad (24)$$

is the effective shear viscosity.

Our model differs from most of the viscoplastic constitutive laws in that it allows for viscous flow at stresses below the critical yield, although with much higher viscosity. This is consistent with experimental data

showing that viscous strains would accumulate at both high and low stresses (Crook et al., 2008; Makhnenko & Podladchikov, 2018). Plasticity onset reduces bulk and shear viscosities significantly, leading to enhanced deformation rates (see Figure 3). Shear and bulk strain rates depend on both effective pressure and shear stress. Increasing τ leads to increased compaction rates (Figure 3a) and further reduction of effective bulk viscosity (Figure 3b). This is known as shear-enhanced compaction and is observed in creep experiments as well as in the usual triaxial compaction tests (Skurtveit et al., 2013; Xiao et al., 2006; Xiao & Evans, 2003; Zhu et al., 1997). As in other viscoplastic models, more complicated hardening laws and more nonlinearities can be introduced.

3.3. Compaction-Dilation Boundary

In our model, the transition from compaction to dilation depends on the interplay between elastic, plastic, and rate-dependent deformation. For rate-dependent deformation, the compaction-dilation boundary can be directly found from Equation 16 by putting $\dot{\varepsilon}^r=0$. For the simplest considered case of $m = 2$ and $\alpha_\tau = 0$, the compaction-dilation boundary will be defined as

$$\left(2\frac{\Lambda\eta_b f}{Y^2}\exp\left(\frac{f}{Y}\right) + 1\right)p_e - 2\Lambda\eta_b f \exp\left(\frac{f}{Y}\right)\frac{p_0}{Y^2} = 0. \quad (25)$$

As f depends on both p_e and τ , this defines a nonlinear curve, which closely follows the failure envelope at $p_e < Y$. It is shown as a thick black curve in Figure 3a. As effective pressure increases further, the compaction-dilation boundary follows a straight line, which will be vertical in the case of $\alpha_\tau = 0$ and more inclined at higher values of α_τ .

The onset of dilation at positive effective pressures is due to the presence of shear stresses. This is known as shear-induced dilation, which is commonly observed in compaction experiments (e.g., Makhnenko & Labuz, 2015; Vajdova et al., 2004). Several groups have recently performed studies involving multiload triaxial creep tests on various rock types (e.g., Sabitova et al., 2019; Tsai et al., 2008; Zhang et al., 2016). In these experiments, the axial stress is applied stepwise to cylindrical rock samples while the lateral confinement is held constant. After each load increment, the specimen is allowed to creep for a time interval ranging from hours to days, during which deformations are continuously monitored. The experimental results show that the volumetric strain curves exhibit volumetric compaction at low stresses, followed by dilatancy at higher stresses. The strain rate during compaction is smaller than the strain rate during dilation. Moreover, significant strains were developed during dilation before macroscopic failure of the sample (e.g., Sabitova et al., 2019; Tsai et al., 2008). These results support our model, which predicts viscous dilation at positive effective pressures and leads to compaction/decompaction asymmetry.

4. Comparison With Experimental Data

4.1. Compaction Data

We aim to derive viscoelastoplastic constitutive equations to model the rheology of geological media with applications to fluid flow in mind. However, before we proceed further to fluid flow applications, we compare the derived yield surface and compaction relations with some of the available laboratory results. In this paper, we do not aim for complete experimental verification of our model, which would require a good dataset with compaction and creep data on the same material under various relevant loading conditions. This lies outside the scope of the present paper. Most of the rock mechanical tests in the literature are performed under triaxial conditions. Very few papers present plane strain results (Makhnenko & Labuz, 2014; Makhnenko & Labuz, 2016). Thus, for comparison, we choose compaction data from triaxial experiments from the literature (Baud et al., 2006; Tsai et al., 2008). In compaction triaxial experiments, a cylindrical sample is initially loaded hydrostatically ($\sigma_1 = \sigma_2 = \sigma_3$) at drained conditions until the desired level of confining pressure $p_c = \sigma_2 = \sigma_3$ is reached. After that, p_c is kept constant and only axial load σ_1 is further increased to facilitate shear loading so that $\sigma_1 > \sigma_2 = \sigma_3$. The mean effective stress and the differential stress measured in experiments correspond to our p_e and $\tau = \sigma_1 - \sigma_3$, respectively. Volumetric deformation in compaction experiments is estimated as porosity reduction $\varepsilon = (\varphi_0 - \varphi) \cdot 100\%$. In our model, the compaction relation for the triaxial stress conditions takes the form (see Appendix B for derivation)

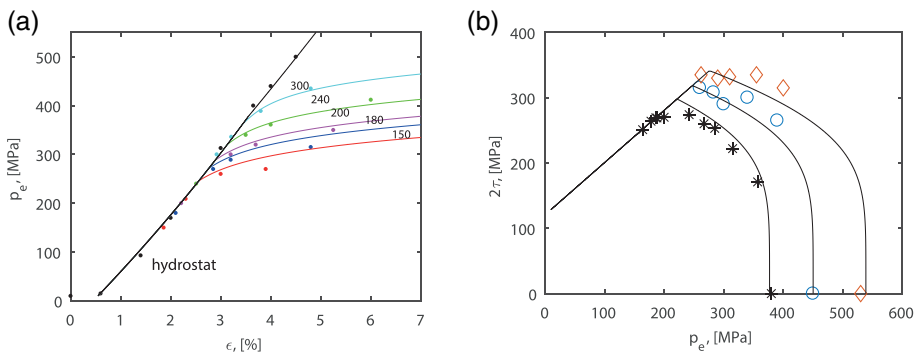


Figure 4. (a) Modeling predictions (solid lines) versus data (dots) for compaction of Darley Dale sandstone with an initial porosity of 13% taken from Baud et al. (2006). For nonhydrostatic curves, confining pressures were kept constant at values indicated next to each curve (in MPa). (b) Comparison between theoretical yield surface and experimental data on the initial yield stress and evolution of the yield stress as a function of the plastic volumetric strain for Darley Dale sandstone taken from Baud et al. (2006). Theoretical curves are shown as solid lines, and data are represented with asterisks ($\varepsilon^p = 0$), circles ($\varepsilon^p = 0.1\%$), and diamonds ($\varepsilon^p = 0.25\%$). Dotted colored lines correspond to the stress path during triaxial experiments. The color code is the same as in Figure 4a.

$$\dot{\varepsilon}^p = - \left(\frac{\partial F}{\partial \varepsilon^p} \right)^{-1} \left(\frac{\partial F}{\partial p_e} \frac{dp_e}{dt} + \frac{\partial F}{\partial \tau} \frac{d\tau}{dt} \right). \quad (26)$$

In triaxial experiments, loading follows a specific trajectory in the plane, so that

$$\frac{d\tau}{dp_e} = \begin{cases} 0, & \sigma_1 = \sigma_2 = \sigma_3 < p_c \\ 3/2, & \sigma_1 > \sigma_2 = \sigma_3 = p_c \end{cases} \quad (27)$$

Substituting Equations 8 and 27 into Equation 26, one obtains the following compaction relation, which might be used directly for the description of experimental results:

$$\dot{\varepsilon}^p = \frac{3\varphi}{2h} \exp \left(\left(\frac{p_e - \alpha_\tau \tau - p_0}{Y} \right)^m - 1 \right) \frac{dp_e}{dt} \cdot \left[m \left(1 + \left(\frac{\tau}{\tau_0} \right)^n \right) \left(\frac{2}{3} - \alpha_\tau \right) \left(\frac{p_e - \alpha_\tau \tau - p_0}{Y} \right)^{m-1} + n \frac{Y}{\tau_0} \left(\frac{\tau}{\tau_0} \right)^{n-1} \right] \quad (28)$$

In the hydrostatic limit, this it reduces to

$$\dot{\varepsilon}^p = m \frac{3\varphi}{2h} \left(\frac{2}{3} - \alpha_\tau \right) \exp \left(\left(\frac{p_e - p_0}{Y} \right)^m - 1 \right) \left(\frac{p_e - p_0}{Y} \right)^{m-1} \frac{dp_e}{dt} \quad (29)$$

These compaction equations and this failure envelope were implemented into MATLAB code, which is used further for comparison of theoretical results with experimental data.

The experimental data that we use for comparison with model output were taken from Baud et al. (2006). They describe the compaction of Darley Dale sandstone with an initial porosity of 13% (see Figure 2a in (Baud et al., 2000)). Hydrostatic compaction was performed at effective pressures up to 500 MPa. Five non-hydrostatic curves were obtained by initial hydrostatic loading up to 150, 180, 200, 240, and 300 MPa, with confining pressure, p_c , kept constant at these levels (Figure 4). At low effective mean stress, data show a non-linear rapid compaction, which might be explained by the closure of microcracks. A crack porosity can be introduced here to capture this portion of a compaction curve (Shapiro, 2003). For simplicity, we do not model an exact compaction trend below the crack closure pressure. Instead, we approximate this stage with almost instant porosity reduction, assuming that the elastic compaction of stiff porosity starts after $\varepsilon = 0.75\%$. After crack closure pressure, hydrostatic compaction data show almost linear dependence of volumetric

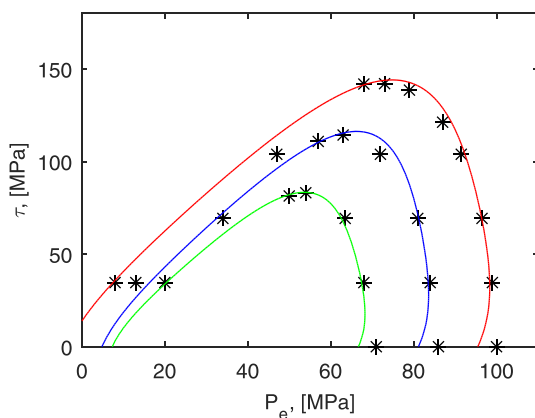


Figure 5. Modeling predictions (solid lines) versus experimental data (asterisk) for viscous plastic potentials of Mushan sandstone with an initial porosity of 14.1% taken from Tsai et al. (2008).

deformation on effective pressure until pore collapse slightly enhances the compaction rate, leading to nonlinearity beyond critical stress $p^* = 380 \text{ MPa}$ (black stars in Figure 4). The presence of shear stresses reduces the critical stress for the onset of pore collapse and significantly influences the slope of the compaction curves. Compaction data from Baud et al. (2006) are supplemented by experimental failure envelopes shown in Figure 4b with an asterisk ($\varepsilon^p = 0$), circles ($\varepsilon^p = 0.1\%$), and diamonds ($\varepsilon^p = 0.25\%$) for different levels of accumulated volumetric plastic strain. The best fit for all experimental curves was obtained using $G = 1.4 \text{ GPa}$, $Y = 190 \text{ MPa}$, $p_0 = 190 \text{ MPa}$, $\tau_0 = 128 \text{ MPa}$, $n = 5$, $m = 1$, $\alpha_\tau = 0.2$, and $h = 12.5 \text{ GPa}$. Figure 4 shows theoretical predictions (solid lines) plotted on top of the respective data points for six compaction curves corresponding to different levels of confining pressure and three failure envelopes corresponding to three different levels of accumulated plastic strain. Note that once fracturing or strain localization is initiated, full 2-D or 3-D numerical simulations of elastoplastic deformation and elastic unloading are required to describe the experimental results (Stefanov et al., 2011).

4.2. Viscous Creep Data

Viscous, or time-dependent, deformation of porous rocks is studied in a number of triaxial creep experiments recently summarized in a review paper from Brantut et al. (2013). These studies show that time-dependent deformation can be very significant in shales, rock salt, tuff, sandstones, and limestones but also present in hard rocks such as granite and basalt. Most of the creep experimental studies focused on stress-strain-time behavior and the influence of temperature and a pore fluid chemistry on creep. Some studies also report axial creep strain rates as a function of applied stresses (Brantut et al., 2013; Heap et al., 2015; Rybacki et al., 2015). The works of Zhang et al. (2015), Makhnenko and Podladchikov (2018), and Sabitova et al. (2019) report volumetric strain rates. Relatively few studies focus on characterizing the yield surface and viscous plastic potentials (Maranini & Brignoli, 1999; Tsai et al., 2008; Weng et al., 2010).

In most of the materials, development of the creep strain in time is characterized by three distinct stages: the primary, or transient, creep phase with strain rate decreasing with time; the secondary, or stationary, creep phase with a constant (i.e., time-independent) strain rate; and a final, accelerating stage followed by specimen failure. Tsai et al. (2008) performed multistage triaxial creep experiments on dry samples of Mushan sandstone from Taiwan, in which both volumetric strain and shear strain were measured. Experiments were performed under a constant room temperature and the time of each experiment was adjusted so that the stationary creep stage was reached. Elastic deformation was carefully subtracted from the total strain by using loading-unloading-reloading cycles. Vectors of plastic and viscous strain increments were obtained during the short-term and creep stages of experiments, respectively, and plotted on the (p_e, τ) -plane. After that, plastic and viscous potential surfaces were plotted, assuming that they are normal to the direction of the strain increments. Tsai et al. (2008) showed that obtained viscous plastic potential has the same functional form as the plastic potential and yield surface. Maranini and Brignoli (1999) also documented the viscous plastic failure envelope during creep tests on porous limestone, which is very similar to the standard failure envelope. Here, we compare our viscous plastic flow potentials with those obtained by (Tsai et al., 2008). Figure 5 shows a comparison of the experimental data with the theoretical viscous plastic potential defined by Equation 9 with $n = 2$, $m = 2$, and $\alpha_\tau = 0.2$. For the green curve, we used $p_0 = 37 \text{ MPa}$, $Y = 21 \text{ MPa}$, and $\tau_0 = 33 \text{ MPa}$; for the blue curve, we used $p_0 = 43 \text{ MPa}$, $Y = 27 \text{ MPa}$, and $\tau_0 = 46 \text{ MPa}$; and for the red curve, we used $p_0 = 46 \text{ MPa}$, $Y = 35 \text{ MPa}$, and $\tau_0 = 57 \text{ MPa}$. The results show reasonable agreement.

5. Porosity Waves in the Presence of Shear

Porosity waves were suggested to be a fast and efficient fluid transport mechanism forming various focused fluid flow structures (Appold & Nunn, 2002; Barcilon & Richter, 1986; Cai & Bercovici, 2013; Connolly & Podladchikov, 2015; Jordan et al., 2018; McKenzie, 1984; Räss et al., 2014; Richard et al., 2012; Scott & Stevenson, 1984; Yarushina, Podladchikov, et al., 2015). Most of the previous models ignored the

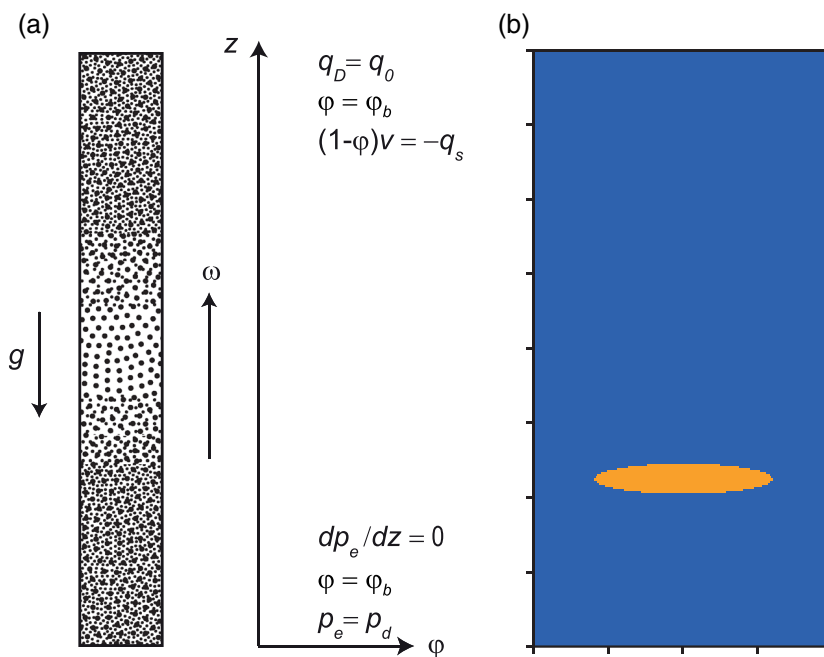


Figure 6. Schematic initial model setup. (a) 1-D steady-state propagation of the porosity wave. A vertical column of porous rock with homogeneous porosity φ_b is subsiding under its own weight, while a steady porosity wave travels upward through the column with velocity ω . (b) 2-D porosity wave formation. The elliptical region of high porosity is located at the lower part of the computational domain of constant background porosity φ_b .

influence of deviatoric stresses on wave propagation, assuming that there is no shear or deviatoric stresses in the rock. Yet, recent numerical models that include full mechanical formulation with all components of the stress tensor show that propagation of porosity waves is also associated with changes in shear stresses, especially ahead of the wave head (Omlin et al., 2018). However, these models used ad hoc rheology with decompression weakening only. Here, we investigate how derived rheology influences the propagation of porosity waves. First, we consider the 1-D steady-state compactioning porous column and derive an analytical solution for purely viscous and viscoplastic porosity waves in the presence of shear. After that, we look at the transient 2-D numerical solution for porosity waves in a medium, which viscoplastic behavior is described by using the constitutive equations derived above.

5.1. 1-D Steady-State Viscous Solution With Shear

We consider equilibrium compaction or uniform sedimentation of a vertical column of fluid-saturated porous rock. During sedimentation, low-density fluid segregates from the deformable porous matrix. Over time, compaction in the upper part of the sedimentary column evolves toward a steady state, while the porosity profile becomes independent of time and forms a stationary porosity wave (Figure 6a). One-dimensional stationary solutions can be obtained by putting $\partial/\partial t = 0$ and replacing material time derivatives with $d/dt = v\partial/\partial z$, where $v = v(z)$ is a vertical component of solid velocity. Deviatoric stresses are present in the media. In our derivation of the one-dimensional steady-state solution, we follow the same procedures as in previous publications from Connolly and Podladchikov (2000) and Yarushina, Podladchikov, and Connolly (2015), which provide them in more detail. Here, we offer a brief summary of the governing equations and show how they are modified in the presence of shear.

Mass conservation for fluid and solid phases gives the following nontrivial components of the solid velocity and Darcy flux:

$$v(z) = -\frac{q_s}{1-\varphi}, \quad q_D(z) = q_s \frac{\varphi - \varphi_b}{(1-\varphi)(1-\varphi_b)} + q_0 \quad (30)$$

where φ_b is the constant background porosity, q_s is the sedimentation rate, and q_0 is the background Darcy

flux. The force balance equation in the presence of shear slightly changes in comparison to the hydrostatic case and gives

$$\frac{d\tau_z}{dz} - \frac{d\bar{p}}{dz} - g\bar{\rho} = 0 \quad (31)$$

where τ_z is the vertical deviatoric stress, g is the gravity, and $\bar{\rho} = \rho_f\varphi + \rho_s(1-\varphi)$ is the total density. The only nontrivial component of the shear stresses can be related to the vertical velocity using the linear viscous law:

$$\tau_z = \frac{4}{3}\eta_s \frac{dv}{dz} \quad (32)$$

and, thus, the total force balance becomes

$$\frac{4}{3}\eta_s \frac{d^2v}{dz^2} - \frac{d\bar{p}}{dz} - g\bar{\rho} = 0 \quad (33)$$

At the remote boundary, we assume the lithostatic pressure gradient, that is, $\bar{p}'(z = \infty) = -g\bar{\rho}$. Equation 33 must be complemented by the Darcy law

$$q_D = -\frac{k}{\mu} \left(\frac{dp_f}{dz} + g\rho_f \right) \quad (34)$$

where k is permeability, μ is fluid shear viscosity, and p_f and ρ_f are the pressure and density of the fluid. Introducing effective pressure p_e and using Equation 30, the Darcy law may be written in the form

$$q_s \frac{\varphi - \varphi_b}{(1-\varphi)(1-\varphi_b)} + q_0 = -\frac{k}{\mu} \left(\frac{d\bar{p}}{dz} - \frac{dp_e}{dz} + g\rho_f \right) \quad (35)$$

We assume that, at the remote boundary, $dp_e/dz = 0$; thus, from Equation 35, it follows that

$$q_0 = g\Delta_\rho \frac{k_b}{\mu} (1 - \varphi_b) \quad (36)$$

where k_b is the constant background permeability and $\Delta_\rho = \rho_s - \rho_f$ is the difference between solid and fluid densities. Combining Equations 35 and 33, we arrive at the following hydraulic equation:

$$\frac{dp_e}{dz} = \frac{4}{3}\eta_s \frac{d^2v}{dz^2} + \frac{\mu q_s}{k} \frac{\varphi - \varphi_b}{(1-\varphi_b)(1-\varphi)} - g\Delta_\rho (1 - \varphi) \left(1 - \frac{k_b}{k} \right) \quad (37)$$

In the limit of $d^2v/dz^2 \rightarrow 0$, it coincides with the hydraulic equation from the models of Connolly and Podladchikov (2007) and Yarushina, Podladchikov, and Connolly (2015). This equation must be solved together with Equation 30 for solid velocity and the equation for viscous compaction:

$$\frac{d\varphi}{dz} = -\frac{\varphi}{\eta_b} p_e \quad (38)$$

Assuming power law porosity-permeability dependence

$$k = k_b \left(\frac{\varphi}{\varphi_b} \right)^v \quad (39)$$

Equations 37–39 can be combined into a single ordinary differential equation, the so-called phase portrait equation:

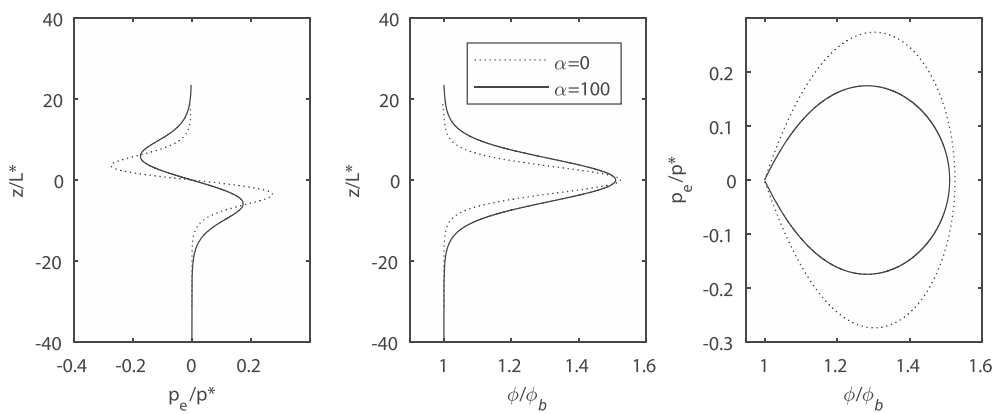


Figure 7. Analytic stationary solution ($\varphi_b = 0.01$, $v = 3$, $\omega = 4$) for the porosity and effective pressure distribution within solitary porosity waves in purely viscous rocks in the presence of shear stresses ($\alpha = 100$). Reference solution without shear ($\alpha = 0$) is presented with a dotted line.

$$\frac{\varphi(1 + \varphi\alpha)}{\omega} \frac{p_e}{(p^*)^2} \frac{dp_e}{d\varphi} = \omega \frac{\varphi - \varphi_b}{\varphi_b} \left(\frac{\varphi}{\varphi_b}\right)^{-v} + \left(\frac{\varphi}{\varphi_b}\right)^{-v} - \frac{\varphi\alpha}{\omega} \left(\frac{p_e}{p^*}\right)^2 - 1 \quad (40)$$

where

$$p^* = \Delta_\rho g \sqrt{\frac{\eta_b k_b}{\mu \varphi_b}} \quad (41)$$

is the characteristic pressure scale,

$$\omega = q_s \frac{\mu \varphi_b}{\Delta_\rho g k_b} \quad (42)$$

is a nondimensional speed of the porosity wave, and

$$\alpha = \frac{4\eta_s}{3\eta_b} \quad (43)$$

is the ratio of shear and bulk viscosities. Its solution is given by the following expression:

$$(1 + \alpha\varphi)^2 \frac{p_e^2}{2\omega(p^*)^2} + \ln \frac{\varphi}{\varphi_b} - \frac{\omega - 1}{v} \left(\frac{\varphi}{\varphi_b}\right)^{-v} + \frac{\omega - \alpha\varphi_b(\omega - 1)}{v - 1} \left(\frac{\varphi}{\varphi_b}\right)^{1-v} + \frac{\alpha\varphi_b}{v - 2} \left(\frac{\varphi}{\varphi_b}\right)^{2-v} + \alpha\varphi - \omega \frac{\alpha\varphi_b v + v - 2}{v(v - 1)(v - 2)} - \frac{\alpha\varphi_b v^2 + v - 1}{v(v - 1)} = 0 \quad (44)$$

Equation 44 coincides with the solution previously given by Yarushina, Podladchikov, and Connolly (2015) if $\alpha = 0$. Depth profiles of porosity and pressure may be obtained numerically by solving coupled ordinary differential equations

$$L^* \frac{d\varphi}{dz} = \frac{\varphi p_e}{\omega p^*} \quad (45)$$

$$(1 + \alpha\varphi) \frac{L^*}{p^*} \frac{dp_e}{dz} = \frac{\varphi - \varphi_b}{\varphi_b} \left(\frac{\varphi}{\varphi_b}\right)^v \omega + \left(\frac{\varphi}{\varphi_b}\right)^v - 1 - \frac{\alpha\varphi}{\omega} \frac{p_e^2}{(p^*)^2} \quad (46)$$

where

$$L^* = \sqrt{\frac{\eta_b k_b}{\mu \varphi_b}} \quad (47)$$

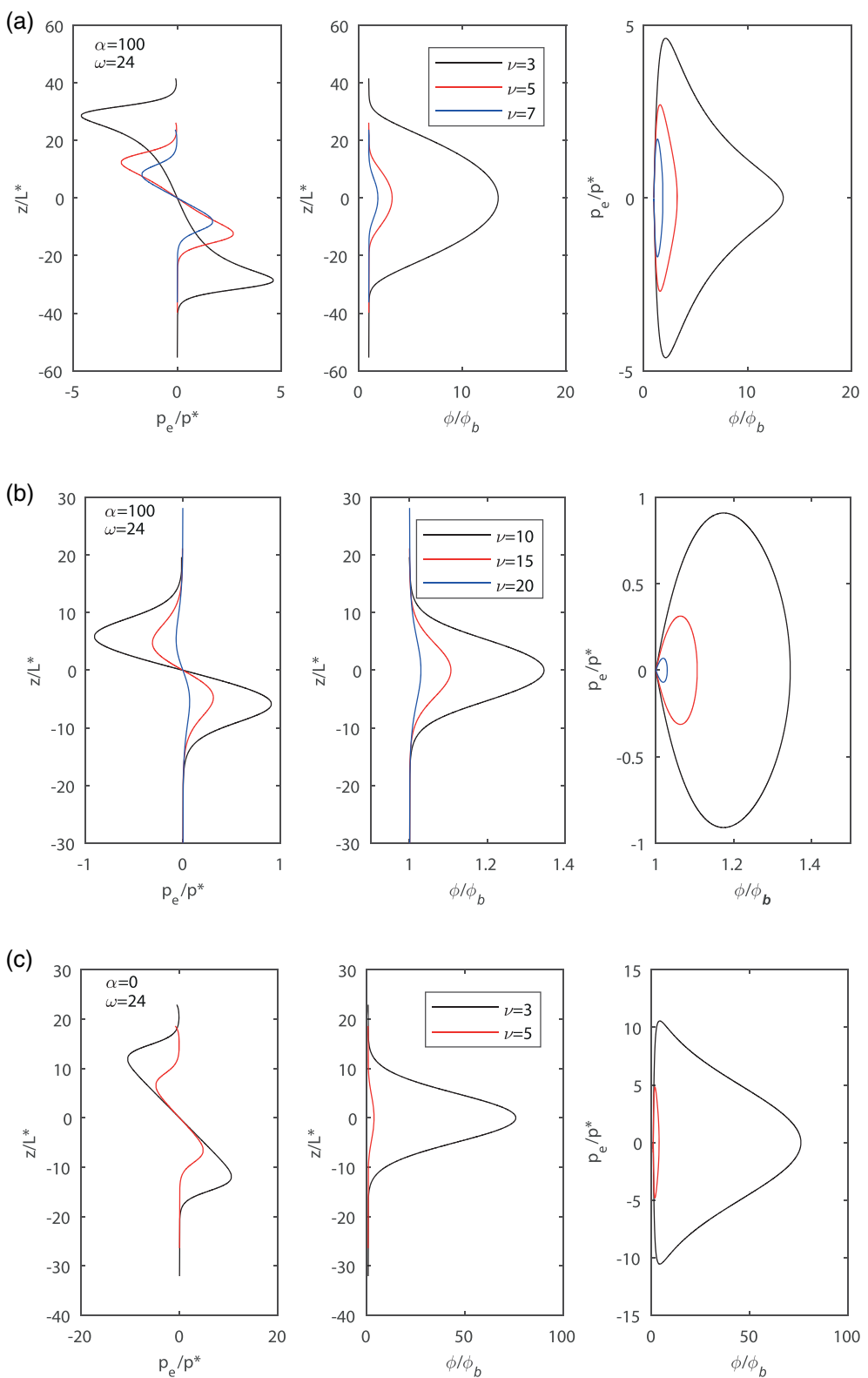


Figure 8. Combined effect of ν and ω on purely viscous porosity waves. (a) Large difference between ν and ω in the simulation with the effect of shear. (b) Small difference between ν and ω in a simulation with shear. (c) Reference simulation without shear effects at $\alpha = 0$ and the same value of ω . Colors show simulations for different values on ν , as indicated in each figure.

is the compaction length. Figure 7 shows the porosity wave solution to Equations 44–46 for $\alpha = 100$, $\varphi_b = 0.01$, $v = 3$, and $\omega = 4$. The comparison of viscous solutions with shear ($\alpha > 0$) and viscous solutions without shear ($\alpha = 0$) in Figures 7 and 8 shows that shear stresses reduce pressure generated within the porosity wave. The nonlinear dependence of permeability on porosity plays an important role in this reduction, especially for rocks with a strong porosity dependence of permeability (i.e., with high values of v). For example, shales generally have large permeability exponents, in the range $v = 24.9 – 55.5$ (Dong et al., 2010). David et al. (1994) report $v = 4.6 – 25.4$ for five different sandstones. Our results show that for $v = 3$, pressure reduces about two times in the presence of shear (Figure 8a) in comparison to a reference case without shear (Figure 8c). For $v = 20$, pressure is reduced over 30 times in the presence of shear (Figure 8b). Similarly, the amplitude of the wave, that is, the maximum porosity that the wave can reach, is affected by v and the magnitude of the shear stresses. Porosity inside the wave is much higher for rocks with low permeability exponent v , while in rocks with higher v , porosity inside the wave does not increase as much. For example, wave amplitude $\varphi/\varphi_b \approx 13$ for $v = 3$, while it is only $\varphi/\varphi_b \approx 1.3$ for $v = 20$. Yet, implications for permeability change inside the wave can be quite significant, as even a small porosity change inside the wave can increase permeability orders of magnitude at high values of v in Equation 39. It is interesting to note that the presence of shear stresses may also lead to sharp pressure gradients inside the wave (Figure 8a) when the difference between permeability exponent v and nondimensional wave speed ω is too high. These pressure gradients at the pressure front can be responsible for numerical instabilities in the numerical codes based on poroviscoelastic models with full stress tensor, as implemented by Omelin et al. (2018) and Räss et al. (2019). Instabilities in these codes arise at high values of the permeability exponent, which brings strong nonlinearity into the system of equations. Our 1-D calculations for various values of v and ω presented in Figure 8 indicate that it is not high values of v in themselves that cause such problems but, rather, the difference between v and ω . For example, the pressure profile for $v = 20$ looks smoother (Figure 8b) than the pressure profile for $v = 3$ (Figure 8a) for $\omega = 24$.

5.2. 1-D Steady-State Viscoplastic Solution With Shear

Now we will investigate how plastic deformation alters porosity wave propagation. As in the previous section, we will look at the upward rising porosity wave in a setup shown in Figure 6a. The only driving force is buoyancy arising due to the fluid being less dense than the rock. All previous porosity wave solutions assumed explicitly or implicitly that $p_e = 0$ at the remote boundary (e.g., Connolly & Podladchikov, 2007; Rice, 1992). We relax this assumption by allowing fluid pressures to be smaller than lithostatic and assuming, instead, that $p_e = p_d > 0$ at the remote boundary, that is, effective pressure corresponds to the dilation pressure in our viscoplastic constitutive law given by Equations 20 and 21. This assumption is still somewhat idealistic; in the future, other boundary conditions must be tested.

Rising fluid pressure at the top of the wave will induce viscoplastic failure leading to dilation, even at positive effective pressures. At the lower part of the wave, pressures are reduced and, thus, will fall into the purely viscous domain. This will lead to compaction-decompaction asymmetry, where different constitutive laws will describe the compacting and dilating parts of the wave. Most of the derivations of the previous section will be valid for the viscoplastic case. In the compaction domain, that is, at $p_e > p_d$, the viscous porosity Equation 38 from the previous section will still hold, and pressure and porosity evolution will be given by Equations 40, 45, and 46 from the previous section. With a new nontrivial pressure boundary condition $p_e(\varphi_b) = p_d$ at the remote boundary, the solution to Equation 40 will take the form

$$\begin{aligned} (1 + \alpha\varphi)^2 \frac{p_e^2}{2\omega(p^*)^2} - (1 + \alpha\varphi_b)^2 \frac{p_d^2}{2\omega(p^*)^2} + \ln \frac{\varphi}{\varphi_b} = \\ = \left(\frac{\varphi}{\varphi_b} \right)^{-v} \frac{\omega - 1}{v} - \frac{\omega - \alpha\varphi_b(\omega - 1)}{v - 1} \left(\frac{\varphi}{\varphi_b} \right)^{1-v} - \frac{\omega\alpha\varphi_b}{v - 2} \left(\frac{\varphi}{\varphi_b} \right)^{2-v} - \\ \alpha\varphi + \alpha\varphi_b \frac{v^2 - 2v + \omega}{(v - 1)(v - 2)} + \frac{v + \omega - 1}{v(v - 1)} \end{aligned} \quad (48)$$

In the dilating part of the wave, the viscoplastic compaction Equation 20 might be used to obtain the porosity equation of the form

$$\nu \frac{d\varphi}{dz} = \varphi \frac{p_e - p_d}{\eta_{eff}} \quad (49)$$

For simplicity, we assume that η_{eff} and p_d are constant. The first assumption means that in Equation 5, changes in porosity are ignored. The second assumption means that the compaction/dilation boundary is approximated with a vertical straight line in the plastic domain (see Figure 3a), that is, that an elaborate expression for p_d in Equation 23 is approximated with a constant value. This is reasonable for $\alpha_\tau = 0$ in Equation 8. In the next section, we present a numerical solution that includes the full dependency on pressure and shear stress. Here, we want to explore how the introduction of plasticity and dilatancy at positive pressures affects the porosity waves. Equation 37 does not include assumptions about the rheology of the rock and can be used to derive the hydraulic equation. Substituting Equation 49 into Equations 30 and 37 gives

$$(1 + \alpha\varphi) \frac{L^*}{p^*} \frac{dp_e}{dz} = \frac{\varphi\omega - \varphi_b(\omega - 1)}{\varphi_b} \left(\frac{\varphi}{\varphi_b} \right)^v - 1 - \frac{\alpha\varphi}{\omega} \frac{(p_e - p_d)^2}{(p^*)^2} \quad (50)$$

The porosity Equation 49 can be rewritten in the following nondimensional form:

$$L^* \frac{d\varphi}{dz} = \frac{\varphi}{\omega} \frac{p_e - p_d}{p^*} \quad (51)$$

Excluding z from these equations, we obtain

$$\frac{\varphi(1 + \alpha\varphi)}{\omega} \frac{p_e - p_d}{(p^*)^2} \frac{dp_e}{d\varphi} = \frac{\varphi\omega - \varphi_b(\omega - 1)}{\varphi_b} \left(\frac{\varphi}{\varphi_b} \right)^v - 1 - \frac{\alpha\varphi}{\omega} \frac{(p_e - p_d)^2}{(p^*)^2} \quad (52)$$

Integration of the last equation provides an analytical solution for the phase diagrams at $p_e \leq p_d$, namely,

$$\begin{aligned} \frac{(1 + \alpha\varphi)^2}{2\omega} \frac{(p_e - p_d)^2}{(p^*)^2} + \ln \frac{\varphi}{\varphi_b} &= \\ &= \left(\frac{\varphi}{\varphi_b} \right)^{-v} \frac{\omega - 1}{v} - \frac{\omega - \alpha\varphi_b(\omega - 1)}{v - 1} \left(\frac{\varphi}{\varphi_b} \right)^{1-v} - \frac{\omega\alpha\varphi_b}{v - 2} \left(\frac{\varphi}{\varphi_b} \right)^{2-v} - \\ &\quad - \alpha\varphi + \alpha\varphi_b \frac{v^2 - 2v + \omega}{(v - 1)(v - 2)} + \frac{v + \omega - 1}{v(v - 1)} \end{aligned} \quad (53)$$

The viscoplastic porosity wave solution is presented in Figure 9. It shows that the onset of dilatancy at critical pressure p_d significantly alters the porosity and pressure in comparison with a purely viscous solution. As decompression plastic viscosity is much smaller than purely viscous compaction viscosity (Figure 3), the wave becomes asymmetric, which in 2-D leads to the generation of elongated channels, as we show in the next section. Most importantly, the effective pressures associated with the porosity wave propagation remain positive, that is, generation of a porosity wave in viscoplastic rocks is possible at fluid pressures below the lithostatic stress.

5.3. 2-D Viscoplastic Numerical Solution

We implemented derived rate-dependent constitutive equations into 2-D numerical code for porous flow in deformable porous viscoplastic rocks using the model formulation from (Yarushina & Podladchikov, 2015). Our numerical solution ignores elastic deformation. We used the same numerical scheme as described in (Omlin et al., 2018; Poliakov et al., 1993; Räss et al., 2019). The code is available online (at <https://doi.pangaea.de/10.1594/PANGAEA.909658>). As an initial setup, we use a rectangular domain of viscoplastic deformable porous rock, containing an elliptical high-porosity inclusion in the lower part of the domain formed by, for example, partial melting in magmatic rocks, petroleum generation in source rocks, or dehydration reactions in metamorphic rocks (Figure 6b). Inside the inclusion, the initial porosity is three times higher than the background value, $\varphi_b = 0.05$. Note that unless inertial (e.g., wave propagation) or elastic processes are involved, fluid flow problems in viscoplastic media do not require initial conditions for pressures. Thus, we do not prescribe any specific values for either fluid or effective pressures. The size of the

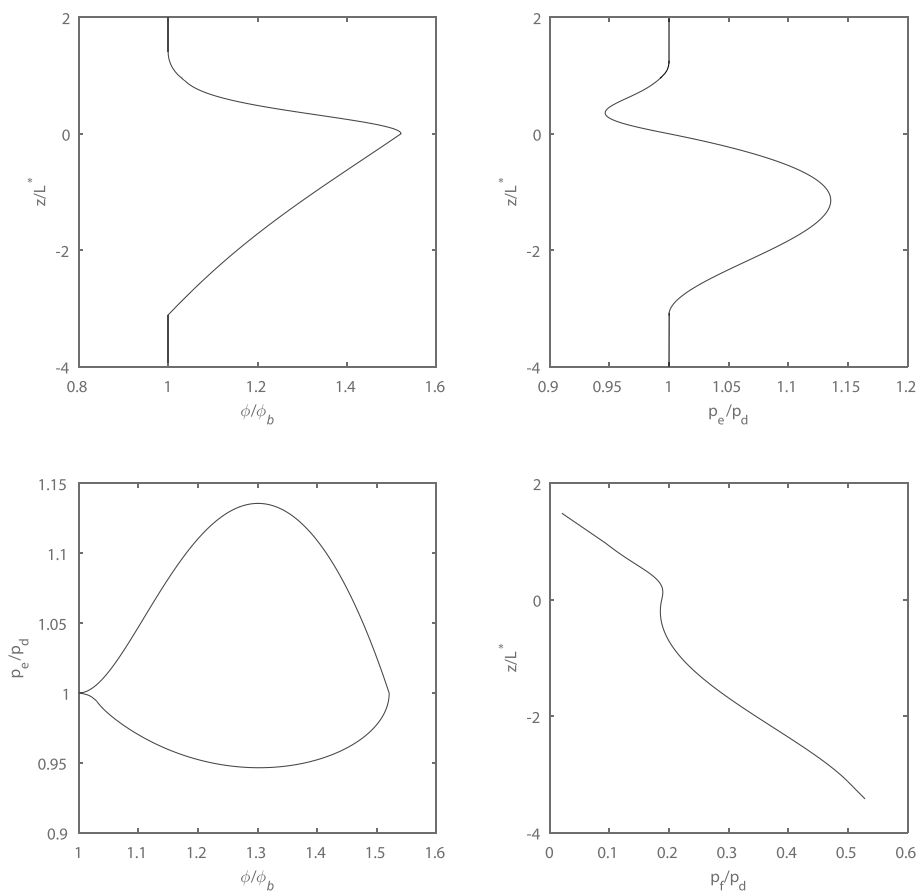


Figure 9. Steady-state depth profiles showing the evolution of porosity, effective pressure, and fluid pressure in viscoplastic porosity waves with $\varphi_b = 0.01$, $v = 3$, $\omega = 4$, $p_d = p_e/2$, $\alpha = 1$, and $\eta_{eff} = \eta_b/100$.

computational domain is 20×40 with the unit of compaction length. We impose free-slip boundary conditions for the solid velocities (no shear stress and zero normal velocity). For the fluid flow problem, we assign no flux conditions on the lateral boundaries and constant inflow (bottom) and outflow (top). The only external force acting on the domain is gravity pointing downward. The parameters used in our 2-D simulations are summarized in Table 2.

Table 2
Nondimensional Simulation Parameters

Parameter	Value
φ_b	0.05
ρ_s	2
ρ_f	1
κ_b	1
μ	1
v	3
η_b	1
C	10
k_0	2
p_0	2.7
n	2
m	2
α_τ	0
τ_0	0.8
Λ	10

To compare the results of our model with those of previous studies, we conduct numerical simulations with both viscoplastic and viscous bilinear rheology. Figure 10a shows channels formed in bilinear viscous rocks with a compaction viscosity 100 times higher than the decompression viscosity. The 2-D simulation results show that our new viscoplastic rheology also leads to the formation of elongated tubular channels (Figure 10b), which are very similar to channels formed in bilinear viscous rocks with decompression weakening, where the ratio of compaction/decompression viscosities is $R = 100$. The rheological asymmetry in the viscoplastic case is caused by a viscoplastic failure at elevated fluid pressures (low effective pressures). It is interesting to note that no negative effective pressure is observed during channel propagation in viscoplastic rocks (Figure 10b). This is related to the new viscoplastic constitutive relations given by Equation 20, which cause dilation of the rock at $p_e = p_d$, reducing pressure buildup above dilation pressure p_d . The results of 2-D numerical simulations also confirm predictions of the 1-D steady-state analytical solution presented in Figure 9, which shows that the effective pressures associated with porosity wave remains positive. This is different from purely viscous

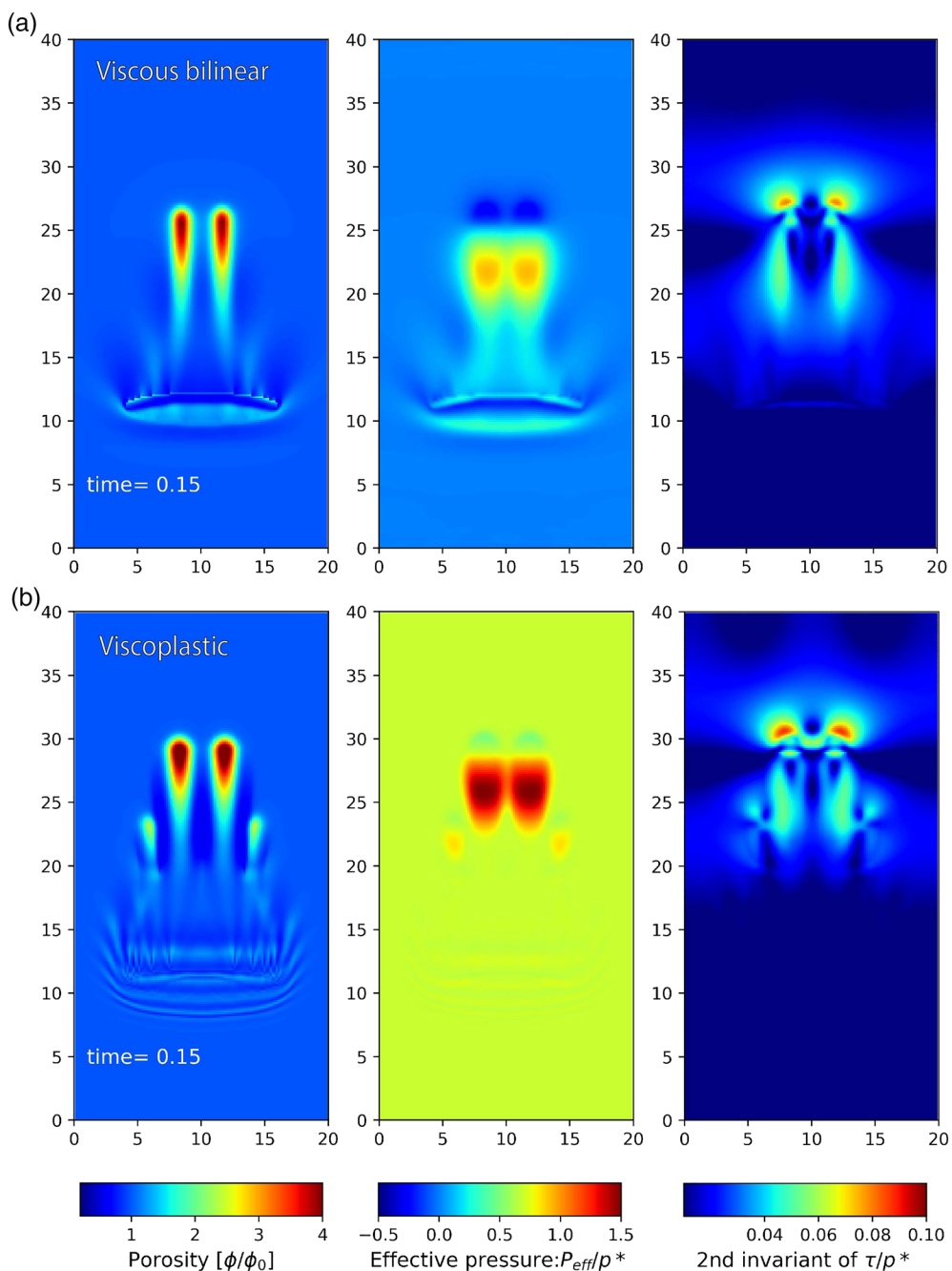


Figure 10. Porosity, effective pressure, and shear stress during propagation of a 2-D porosity wave in bilinear viscous (a) and viscoplastic rocks with shear-dependent bulk rheology. (b) Channels with elevated porosity evolve upward during the simulation.

rocks, in which channel propagation requires fluid pressures higher than the total pressure (compare Figures 10a and 10b). Thus, the new rheology leads to the formation of channelized fluid flow without introducing negative effective pressure, as was the case in previous models. Comparing both models at the same time step, we see that the fluid channels are slightly bigger and rise faster in the viscoplastic model than in the viscous bilinear model. This implies that the new viscoplastic rheology promotes fluid channel formation more efficiently than a decompression weakening rheology from previous works with $R = 100$. Another interesting observation is that shear stresses are unevenly distributed during wave propagation in both viscous bilinear and viscoplastic case and, thus, the assumption for the hydrostatic stress state can be very inaccurate in numerical codes.

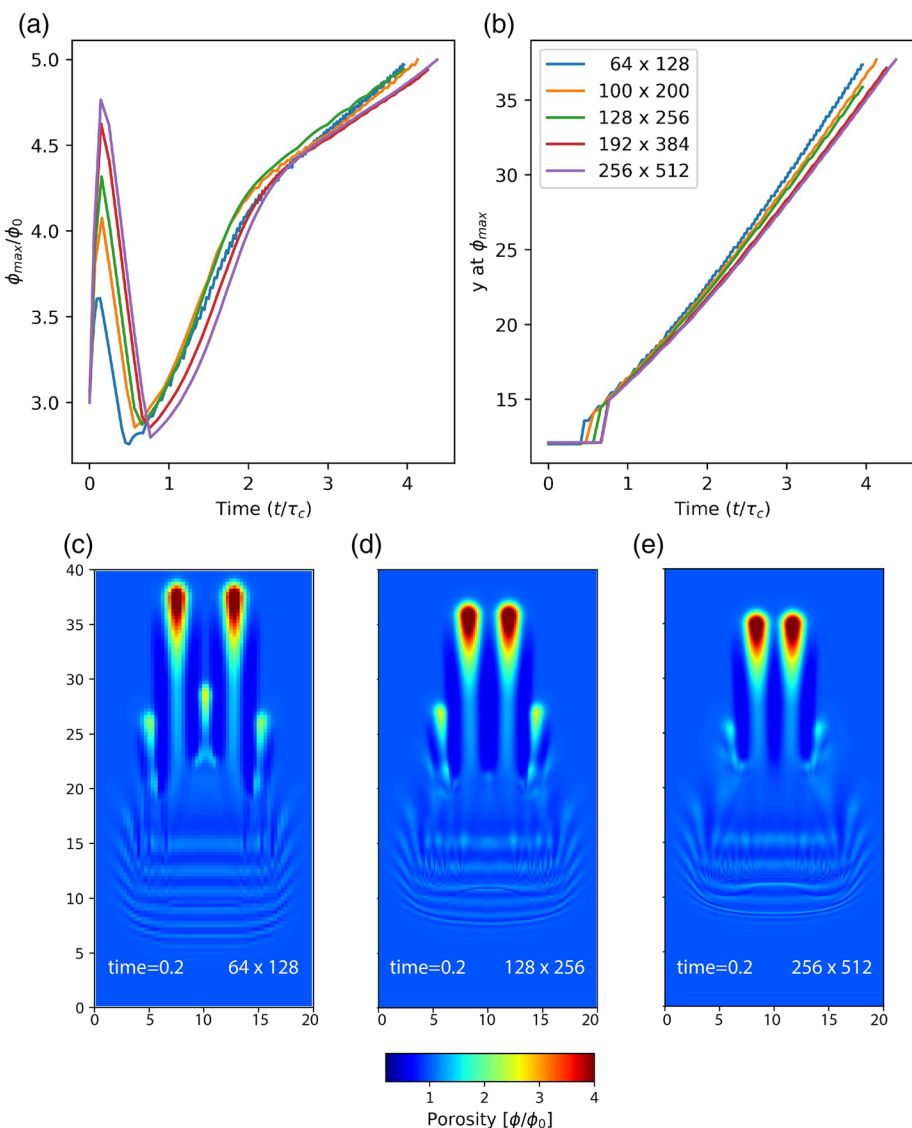


Figure 11. Sensitivity analysis of model results for five grid resolutions. (a, b) The evolution of normalized maximum porosity and position of the wave front through time for all five models. The time is normalized with characteristic timescale $\tau_c = 0.05$. (c–e) The porosity at nondimensional time = 0.2 for models with low (c), intermediate (d), and high resolutions (e).

Five models with different grid resolutions have been run for the sensitivity analysis. The evolution of maximum porosity in the channel (Figure 11a) and the position of the wave front (Figure 11b) show quite similar trends in all the models. The maximum porosity at the initial time steps demonstrates the major difference among the models. This is due to the strong fluid flow within the reservoir at the beginning of the simulation. The lower the resolution is, the bigger the error it introduces. However, little difference can be seen from grid resolution 192×384 to 256×512 . Figures 11c and 11d illustrate the effect of resolution on the porosity evolution. At nondimensional time = 0.2, two major fluid channels form in all three models, and the wave front tends to be higher in the low-resolution model than in the high-resolution model. The runs with low resolution diverge from the correct trend. Three small fluid channels can be seen in the low-resolution model, while only two small channels are found in the other two models. Similar observations were reported for porosity wave solutions by Räss et al. (2019). Thus, considering both the statistical values and model images, our model achieved good convergence when the grid resolution increased.

6. Discussion and Conclusions

An essential feature of our constitutive model is that it builds on the effective media theory. We used an analytical solution for the deformation of a single pore in a nonhydrostatic stress field in our derivation of fully 3-D viscoelastoplastic constitutive laws. Yield surface, flow potential, and compaction relations are obtained by simple volume averaging of an analytical solution. Parameters in the compaction relations are generalized to account for more complex pore geometry. Our model accounts for the (1) stress dependency of material parameters; (2) weakening of the rock with the onset of failure; and (3) possibility of dilatancy at positive effective pressures, that is, shear-induced dilation. The model predictions are compared with experimental data on triaxial mechanical deformation and creep in reservoir rocks. The new model was implemented into 2-D numerical code. New analytical and numerical solutions show that new rheology has serious implications for the propagation of solitary porosity waves.

Porosity waves were previously proposed as a mechanism for generating fast and focused fluid flow in the shallow and deep Earth, which is often evidenced in the form of dikes, veins, pockmarks, mud volcanoes, fluid escape pipes, or gas-conducting chimneys, among other structures. The contrast in the compaction and decompression viscosities is an important parameter that controls the mode of fluid flow focusing on viscously deforming porous rocks (Connolly & Podladchikov, 2007). In rocks with the same compaction and decompression viscosity, fluid flow instability gives rise to porosity waves in the form of spherical blobs. Such blobs can propagate upward as a self-sustained body at a speed that exceeds the background porous fluid flow rate but that is still too inefficient to explain the formation of focused fluid flow structures (Barcilon & Richter, 1986; Mckenzie, 1984; Schmeling, 2000). In rocks with different compaction and decompression viscosities, fluid flow instability leads to the formation of elongated chimney-like structures (Connolly & Podladchikov, 2007; Omlin et al., 2018; Räss et al., 2014; Yarushina, Podladchikov, et al., 2015). The ratio between compaction and decompression viscosity determines the length of the chimney and the speed of its upward propagation. However, compaction/decompression asymmetry in the previous models was achieved in an ad hoc manner by postulating constant but different viscosities at positive and negative effective pressures. Additionally, these models predicted that fluid pressure must exceed lithostatic pressure to produce a porosity wave. These deficiencies limited the success of these models. Our new model also has different compaction and decompression viscosities. However, the difference is achieved naturally as a result of developing plastic failure, as we showed in the previous sections (see Figure 3). Because the transition from compaction to dilation in our model happens at positive effective pressures, fluid pressure does not need to exceed lithostatic pressure to generate a porosity wave. Thus, in our model, porosity waves are a viable mechanism for the generation of focused fluid flow structures. Porosity waves can even compete with hydraulic fracturing, which is often assumed to be responsible for the formation of focused fluid flow (e.g., Arntsen et al., 2007; Bodvarsson et al., 2003). Another application in which the proposed model might be useful is the modeling of shear localization and nonlinear changes in seismic velocity associated with failure processes. This we leave for future work.

Appendix A: Nonhydrostatic Elasto(visco)plastic Deformation of Cylindrical Pores

Often, the choice of an RVE is dictated by available analytical solutions. For compaction and decompression of porous rock under combined pressure and shear loads, cylindrical pore embedded in an infinite incompressible elastoplastic (or viscoplastic) solid that is subject to homogeneous pressure on the pore wall and a couple of far-field compressive or extensional forces ($\sigma_x^\infty \neq \sigma_y^\infty$, $\sigma_{xy}^\infty = 0$) can be considered as an RVE (Figure 1). In the elastic regime, deformation of the pore can be obtained using Kolossof-Muskhelishvili's method of complex potentials, as shown in (Yarushina & Podladchikov, 2007). In the elastoplastic regime, pore collapse is described by the classical analytical solution of Galin (1946), which is extensively discussed in the literature (Chakrabarty, 1987; Kachanov, 1971; Yarushina et al., 2010). Both solutions can be modified to account for the viscous deformation of the solid using the viscoelastic correspondence principle. Changes in pore size and geometry are particularly important for constraining (de)compaction. Thus, here we account only for results reflecting displacements or velocities around the pore. An interested reader can find the full solution with stress distribution in the references above.

A.1 Elastic (Viscous) Deformation of the Pore

In the elastic regime, displacements around the cylindrical pore take the form (Yarushina & Podladchikov, 2007)

$$2Gu_r = p_e \frac{R^2}{r} - \tau R \left(\frac{r}{R} + 2\frac{R}{r} - \frac{R^3}{r^3} \right) \cos 2\theta \quad (\text{A1})$$

$$2Gu_\theta = \tau R \left(\frac{r}{R} + \frac{R^3}{r^3} \right) \sin 2\theta \quad (\text{A2})$$

where G is the elastic shear modulus and

$$\bar{p} = -\frac{\sigma_x^\infty + \sigma_y^\infty}{2}, \quad (\text{A3})$$

$$\tau = \frac{\sigma_y^\infty - \sigma_x^\infty}{2}, \quad (\text{A4})$$

$$p_e = \bar{p} - p_f \quad (\text{A5})$$

are the total pressure prescribed at the far-field boundary, shear stress, and effective pressure, respectively. Due to the mathematical similarity of elastic and viscous problems, the viscous solution can be obtained from Equations A1 and A2 by replacing displacements u_r, u_θ with velocities v_r, v_θ and elastic shear modulus G with shear viscosity η (Goodier, 1936).

A.2 Elastoplastic (Viscoplastic) Deformation of the Pore

With increasing load, the plastic region develops around the pore (Figure 1). This corresponds to grain crushing and pore collapse in laboratory experiments. This moment marks the onset of shear-enhanced compaction. We assume that material around the pore obeys Tresca or von Mises yield criteria, both of which take the form

$$(\sigma_r - \sigma_\theta)^2 + 4\sigma_{r\theta}^2 = 4Y^2, \quad (\text{A6})$$

where Y is the yield stress in pure shear. Plastic yielding begins at the pore boundary when external loads reach critical condition

$$2|\tau| + |p_e| = Y. \quad (\text{A7})$$

When the plastic region fully engulfs the cavity, stresses and displacements in an elastoplastic rock are given by Galin's analytical solution. Here, we use the similarity of pure elastic and pure viscous formulations to modify the classical elastoplastic solution and find stresses and velocities around the cavity in a viscoplastic rock. We consider separately elastic (viscous) and plastic regions.

A.2.1 Solution for the Plastic Zone

Following Galin (1946), we assume that plastic flow in the vicinity of the pore has radial symmetry. In this case, three unknown stress components must satisfy two force balance equations and the yield criterion, which means that stresses can be found without involving any rheological laws. Therefore, stress distribution in the plastic zone is the same for elastoplastic and viscoplastic materials and is given by the following modification of the original Galin's equations:

$$\sigma_r = -p_f - 2Y\xi \ln(r/R) \quad (\text{A8})$$

$$\sigma_\theta = -p_f - 2Y\xi(\ln(r/R) + 1) \quad (\text{A9})$$

$$\sigma_{r\theta} = 0 \quad (\text{A10})$$

where the new plastic limit

$$Y = GY_0/(G - h) \quad (\text{A11})$$

accounts for linear hardening given by parameter h . Without hardening, $h = 0$ and Equations A8 and A9 reduce to classical equations. Here, ξ distinguishes the direction of the load with $\xi = 1$ for compaction and

$\xi = -1$ for decompression. However, no analytical solution in a closed form for displacements in the plastic zone is available for $\sigma_x^\infty \neq \sigma_y^\infty$.

A.2.2 Solution for the Elastic (Viscous) Zone

The solution in the elastic zone is found using Kolossof-Muskhelishvili's method combined with the use of conformal mapping so that (Yarushina et al., 2010)

$$2G(u_x + iu_y) = 2G(u_r + iu_\theta)e^{i\theta} = \varphi(\zeta) - \frac{w(\zeta)}{\overline{w'(\zeta)}}\overline{\varphi'(\zeta)} - \overline{\psi(\zeta)} \quad (\text{A12})$$

where ζ is a complex variable and

$$\varphi(\zeta) = -Y\xi w(\zeta) \left(\ln \frac{w(\zeta)}{R\xi} + \frac{p_f}{2Y\xi} + \frac{1}{2} \right) - \frac{2c\tau}{\zeta} \quad (\text{A13})$$

$$\psi(\zeta) = c \left(\frac{Y\xi}{\zeta} + \tau\zeta \right) \quad (\text{A14})$$

$$w(\zeta) = c \left(\zeta - \frac{\tau}{Y\xi\zeta} \right) \quad (\text{A15})$$

$$c = R \exp \left(\frac{p_e - Y\xi}{2Y\xi} \right) \quad (\text{A16})$$

Due to the mathematical similarity of viscous and elastic problems, Equations A12–A16 can also be used in the viscous zone if displacements and elastic modulus are replaced with viscous counterparts.

The elastoplastic (viscoplastic) solution is valid as long as shear stresses are relatively small (Yarushina et al., 2010). At high effective pressures p_e , the imposed shear load should not exceed approximately 40% of the yield strength ($\tau/Y < \sqrt{2} - 1$). At low effective pressures (approximately), the admissible shear load grows exponentially with scaled effective pressure that guarantees that the cavity is completely enclosed in the plastic boundary:

$$\frac{|P_e|}{2Y} - \frac{1}{2} + \ln \left(1 - \left| \frac{\tau}{Y} \right| \right) \geq 0. \quad (\text{A17})$$

A.2.3 Estimation of the Kinematic Field Within the Plastic Region

Though velocities and displacements in the plastic zone are unknown, some estimations of the relative pore contraction (expansion) can be made if the solid rock is incompressible. The conservation of mass in the solid volume of an RVE requires that

$$\frac{d}{dt} \int_{V_s} \rho dV = - \int_{\Sigma} \rho \mathbf{v} \cdot \mathbf{n} dS \quad (\text{A18})$$

where Σ is the boundary of the solid volume V_s with an outward pointing normal \mathbf{n} , ρ is the constant density, and \mathbf{v} is the velocity vector. For the two-dimensional problem considered here, Equation A18 can be rewritten as follows:

$$\frac{dS_s}{dt} = \frac{d}{dt} \int_{S_s} dS = \oint_{L_s} (-v_y dx + v_x dy) \quad (\text{A19})$$

where S_s is the area occupied by the solid in the (x,y) plane. When the solid contains a cavity, the line integral in A19 is a sum of the integral over the pore boundary L_v and the integral over the external boundary L_{ext}

$$\frac{dS_s}{dt} = - \oint_{L_v} (-v_y dx + v_x dy) + \oint_{L_{ext}} (-v_y dx + v_x dy) = 0 \quad (\text{A20})$$

The first of these integrals represents the flux through the pore with area S_v and also gives changes in the area of the pore dS_v/dt . The second integral is the flux through the total area S . Equation A20 essentially

states that in the incompressible RVE with a single pore, all volume (area) changes are due to pore contraction (expansion). Furthermore, in the incompressible solid, any volume containing the cavity would change by the same amount. In particular,

$$\frac{dS_v}{dt} = \frac{dS_p}{dt} = \oint_L -v_y dx + v_x dy \quad (\text{A21})$$

where S_p is the area enclosed in the elastoplastic (viscoplastic) boundary L (Figure 1). Displacements (velocities for viscoplastic case) at the plastic boundary L can be found from Equations A12 after substitution of complex potentials A13–A15:

$$2G(u_x + iu_y) = Y\xi z \left(2 + \ln \frac{\xi \bar{z}}{\xi z} \right) + \frac{Y^2}{\tau} \bar{z} - 2cY \xi \zeta - c \frac{Y^2 + \tau^2}{\tau} \zeta \quad (\text{A22})$$

To express u_x, u_y through coordinates in the physical z plane, we replaced terms containing $1/\zeta$ and $1/\xi$ using relations

$$\frac{1}{\zeta} = \frac{Y\xi}{c\tau} (c\xi - z), \quad \frac{1}{\xi^2} = \frac{Y^2}{c^2\tau^2} (z^2 - cz\xi) + \frac{Y\xi}{\tau} \quad (\text{A23})$$

that follow from Equation A15. The solution to Equation A15 with respect to ζ gives

$$\zeta = \frac{1}{2c} \left(z \pm \xi \sqrt{z^2 + 4c^2 \frac{\tau}{Y\xi}} \right) \quad (\text{A24})$$

where plus and minus signs describe two different half-planes. On the plastic boundary

$$\frac{(z + \bar{z})^2}{4a^2} - \frac{(z - \bar{z})^2}{4b^2} = 1 \quad (\text{A25})$$

and, therefore, the square root in Equation A24 can be replaced using

$$\pm \sqrt{z^2 + 4c^2 \frac{\tau}{Y\xi}} = \frac{1}{Y^2 - \tau^2} (2Y\tau\bar{z} + \xi(Y^2 + \tau^2)z). \quad (\text{A26})$$

After this operation, Equation A22 on the plastic boundary may be rewritten in the form

$$2G(u_x + iu_y) = zY\xi \ln \left(\frac{\bar{z} Y\xi z + \bar{z}\tau}{z Y\xi \bar{z} + z\tau} \right) - \frac{Y\xi(Y^2 + 3\tau^2)}{Y^2 - \tau^2} z - \frac{4Y^2\tau}{Y^2 - \tau^2} \bar{z}. \quad (\text{A27})$$

To evaluate integral A19, we notice that

$$-u_y dx + u_x dy = -\Im[(u_x + iu_y) d\bar{z}]. \quad (\text{A28})$$

Substitution of A27 into A28 after some algebra leads to

$$\begin{aligned} -u_y dx + u_x dy \Big|_{L_p} &= -c^2 \frac{Y^2 - \tau^2}{2GY} \\ &\cdot \left\{ \frac{2Y\tau(3Y^2 + 5\tau^2)\cos 2\theta + (Y^4 + 12Y^2\tau^2 + 3\tau^4)\xi}{2Y^2\tau^2 \cos 4\theta + 4\tau Y(Y^2 + \tau^2)\xi \cos 2\theta + \tau^4 + Y^4 + 4Y^2\tau^2} + \right. \\ &\left. + 4\tau Y \frac{(Y^2 - \tau^2)\sin 2\theta}{2Y^2\tau^2 \cos 4\theta + 4Y\tau(Y^2 + \tau^2)\xi \cos 2\theta + \tau^4 + Y^4 + 4Y^2\tau^2} \arctan \frac{\tau \sin 2\theta}{Y\xi + \tau \cos 2\theta} \right\} d\theta. \end{aligned} \quad (\text{A29})$$

Taking a contour integral of expression A29 over one quarter of the ellipse gives

$$\oint_{L_p} -u_y dx + u_x dy = 4 \int_{L_p/4} -u_y dx + u_x dy = -\pi c^2 \frac{Y^2 + 5\tau^2}{GY\xi}. \quad (\text{A30})$$

According to A21, dS_v/dt can be obtained by taking time derivatives of both parts in Equation A30 for elastic rocks, leading to

$$\frac{dS_v}{dt} = \frac{d}{dt} \left(-\pi c^2 \frac{Y^2 + 5\tau^2}{GY\xi} \right). \quad (\text{A31})$$

Appendix B: Averaging of the Solution

For a chosen model of RVE, the degree of compaction can be estimated via changes in the pore volume fraction as follows (Yarushina & Podladchikov, 2015):

$$\frac{1}{\varphi} \frac{d\varphi}{dt} = \frac{1}{S_v} \frac{dS_v}{dt}. \quad (\text{B1})$$

B.1 Elastic Compaction

For the circular cavity

$$\frac{dS_v}{dt} = - \left. \int_0^{2\pi} r v_r d\theta \right|_{r=R}. \quad (\text{B2})$$

For elastic rocks, differentiation of radial displacement A1 with respect to time and subsequent substitution into B2 gives

$$\frac{dS_v}{dt} = - \frac{1}{2G} \int_0^{2\pi} \left(\dot{p}_e R^2 - \dot{\tau} R \left(\frac{r^2}{R} + 2R - \frac{R^3}{r^2} \right) \cos 2\theta \right) d\theta = -\pi \frac{\dot{p}_e R^2}{G} \quad (\text{B3})$$

where dot stands for the time derivative. Taking into account that $S_v = \pi R^2$, the porosity equation for poroelastic rocks becomes

$$\frac{G}{\varphi} \frac{d\varphi}{dt} = - \frac{dp_e}{dt}. \quad (\text{B4})$$

Equation B4 implies that, for small elastic deformations around cylindrical pores, shear deformation does not affect porosity. Effective compressibility in poroelastic rocks is a function of porosity only:

$$\frac{1}{K_\varphi} = - \frac{d\varphi}{dp_e} = \frac{\varphi}{G}. \quad (\text{B5})$$

B.2 Viscous Compaction

A viscous compaction relation can be obtained by the substitution of u_r with v_r and G with shear viscosity η_s in Equation B3, resulting in

$$\frac{\eta_s}{\varphi} \frac{d\varphi}{dt} = - p_e. \quad (\text{B6})$$

As in the elastic case, the presence of shear stresses during viscous deformation does not influence compaction. Effective viscosity takes the form

$$\eta_\varphi = - \frac{P_e}{d\varphi/dt} = \frac{\eta_s}{\varphi}. \quad (\text{B7})$$

B.3 Nonhydrostatic Elastoplastic Compaction

For elastoplastic deformation, dS_v/dt is estimated using Equation A31, which, together with $S_v = \pi R^2$, gives the elastoplastic porosity equation in the form

$$\frac{1}{\varphi} \frac{d\varphi}{dt} = - \frac{d}{dt} \left(\frac{c^2 Y^2 + 5\tau^2}{R^2 G Y \xi} \right). \quad (\text{B8})$$

Upon substitution of Equation A16 for c , the elastoplastic compaction relation may be rewritten as

$$\frac{G}{\varphi} \frac{d\varphi}{dt} = - \exp\left(\frac{|p_e|}{Y} - 1\right) \left\{ \left(1 + 5 \frac{\tau^2}{Y^2}\right) \frac{dp_e}{dt} + 10 \frac{\tau}{Y \xi} \frac{d\tau}{dt} \right\} \quad (\text{B9})$$

with effective elastoplastic compressibility

$$\frac{1}{K_\varphi} = \frac{\varphi}{G} \exp\left(\frac{|p_e|}{Y} - 1\right) \left(1 + 5 \frac{\tau^2}{Y^2}\right). \quad (\text{B10})$$

Equation B9 reduces to elastic porosity Equation B4 when there is no shear stress and effective pressure reaches the critical value $|p_e| = Y$ for plasticity onset.

B.4 Nonhydrostatic Viscoplastic Compaction

Replacing displacements and elastic moduli with their viscous counterparts in Equation A30 for the rate of the pore volume change and substituting it into Equation B1, one obtains

$$\frac{1}{\varphi} \frac{d\varphi}{dt} = - \frac{c^2 Y^2 + 5\tau^2}{R^2 \eta_s Y \xi}. \quad (\text{B11})$$

Substitution of c with Equation A16 gives the final form of the viscoplastic porosity equation in the presence of combined pressure and shear loading:

$$\frac{1}{\varphi} \frac{d\varphi}{dt} = - \exp\left(\frac{|p_e|}{Y} - 1\right) \frac{Y^2 + 5\tau^2}{\eta_s Y \xi}. \quad (\text{B12})$$

This equation determines effective viscosity of the form

$$\eta_\varphi = \frac{\eta_s}{\varphi} \frac{Y |p_e|}{Y^2 + 5\tau^2} \exp\left(1 - \frac{|p_e|}{Y}\right). \quad (\text{B13})$$

In the absence of shear, it reproduces the effective viscosity given in our previous work (Yarushina & Podladchikov, 2015).

B.5 Derivation of Yield Criterion

The compaction Equation B9 may be used to derive yield function. For this, we will rewrite elastoplastic constitutive equations for plane strain conditions:

$$\dot{\varepsilon}^p = \dot{\lambda} \frac{\partial Q}{\partial p_e}, \quad \dot{\gamma}^p = \dot{\lambda} \frac{\partial Q}{\partial \tau}. \quad (\text{B14})$$

Plastic multiplier $\dot{\lambda}$ can be found from the consistency condition

$$\frac{\partial F}{\partial p_e} dp_e + \frac{\partial F}{\partial \tau} d\tau + \frac{\partial F}{\partial \varepsilon^p} d\varepsilon^p = 0 \quad (\text{B15})$$

resulting in

$$\dot{\lambda} = - \left(\frac{\partial F}{\partial \varepsilon^p} \frac{\partial Q}{\partial p_e} \right)^{-1} \left(\frac{\partial F}{\partial p_e} \frac{dp_e}{dt} + \frac{\partial F}{\partial \tau} \frac{d\tau}{dt} \right). \quad (\text{B16})$$

Substitution of Equation B16 into B14 gives

$$\dot{\varepsilon}^p = - \left(\frac{\partial F}{\partial \varepsilon^p} \right)^{-1} \left(\frac{\partial F}{\partial p_e} \frac{dp_e}{dt} + \frac{\partial F}{\partial \tau} \frac{d\tau}{dt} \right) \quad (\text{B17})$$

$$\dot{\gamma}^p = - \frac{\partial Q}{\partial \tau} \left(\frac{\partial F}{\partial \varepsilon^p} \frac{\partial Q}{\partial p_e} \right)^{-1} \left(\frac{\partial F}{\partial p_e} \frac{dp_e}{dt} + \frac{\partial F}{\partial \tau} \frac{d\tau}{dt} \right). \quad (\text{B18})$$

Direct comparison of Equations B17 and B9, and subsequent integration of Equation B17 with respect to F , gives yield function of the form

$$F = \left(1 + \left(\frac{\tau}{\tau_0} \right)^n \right) \exp \left(\left| \frac{p_e - \alpha_\tau \tau - p_0}{Y} \right|^m - 1 \right) Y - Y - \frac{h}{\varphi} \varepsilon^p \quad (\text{B19})$$

which gives derived compaction equations if $\tau_0 = Y/\sqrt{5}$, $n = 2$, $m = 1$, $\alpha_\tau = 0$, $p_0 = 0$, and $h = G$. Indeed, substituting Equation B19 into Equation B17, we obtain

$$\dot{\varepsilon}^p = \begin{cases} \frac{\varphi}{h} \exp \left(\frac{p_e}{Y} - 1 \right) \left(\left(1 + \left(\frac{\tau}{\tau_0} \right)^n \right) \frac{dp_e}{dt} + \frac{nY}{\tau} \left(\frac{\tau}{\tau_0} \right)^n \frac{d\tau}{dt} \right) & \text{compaction} \\ -\frac{\varphi}{h} \exp^{-1} \left(\frac{p_e}{Y} + 1 \right) \left(\left(1 + \left(\frac{\tau}{\tau_0} \right)^n \right) \frac{dp_e}{dt} - \frac{nY}{\tau} \left(\frac{\tau}{\tau_0} \right)^n \frac{d\tau}{dt} \right) & \text{decompaction} \end{cases} \quad (\text{B20})$$

Data Availability Statement

Numerical code used to obtain 2-D porosity wave solutions is available online (from <https://doi.pangaea.de/10.1594/PANGAEA.909658>).

Acknowledgments

We are grateful to Guillaume Richard, Jake Jordan, Alexander Minakov, Artem Myasnikov, Sergey Stanchits, Tobias Keller and Yves Bernabe for their helpful comments that improved the quality of the paper. This work was supported by the Norwegian Research Council (Grants 280953 and 280567) and by Russian Ministry of Science and Higher Education (Project 075-15-2019-1890). All the results of the paper can be reproduced following derivations specified in the text.

References

- Angus, D. A., Dutko, M., Kristiansen, T. G., Fisher, Q. J., Kendall, J.-M., Baird, A. F., et al. (2015). Integrated hydro-mechanical and seismic modelling of the Valhall reservoir: A case study of predicting subsidence, AVOA and microseismicity. *Geomechanics for Energy and the Environment*, 2, 32–44.
- Appold, M. S., & Nunn, J. A. (2002). Numerical models of petroleum migration via buoyancy-driven porosity waves in viscously deformable sediments. *Geofluids*, 2(3), 233–247.
- Arntsen, B., Wensaas, L., Loseth, H., & Hermanrud, C. (2007). Seismic modeling of gas chimneys. *Geophysics*, 72(5), Sm251–Sm259. <https://doi.org/10.1190/1.2749570>
- Barcilon, V., & Richter, F. M. (1986). Nonlinear-waves in compacting media. *Journal of Fluid Mechanics*, 164, 429–448. <https://doi.org/10.1017/S0022112086002628>
- Baud, P., Schubnel, A., & Wong, T. F. (2000). Dilatancy, compaction, and failure mode in Solnhofen limestone. *Journal of Geophysical Research*, 105(B8), 19,289–19,303.
- Baud, P., Vajdova, V., & Wong, T. F. (2006). Shear-enhanced compaction and strain localization: Inelastic deformation and constitutive modeling of four porous sandstones. *Journal of Geophysical Research*, 111, B12401. <https://doi.org/10.1029/2005JB004101>
- Bercovici, D., Ricard, Y., & Schubert, G. (2001). A two-phase model for compaction and damage 1. General Theory. *Journal of Geophysical Research*, 106(B5), 8887–8906.
- Biot, M. A. (1941). General theory of three-dimensional consolidation. *Journal of Applied Physics*, 12(2), 155–164.
- Biot, M. A. (1962). Mechanics of deformation and acoustic propagation in porous media. *Journal of Applied Physics*, 33(4), 1482. <https://doi.org/10.1063/1.1728759>
- Boydvarsson, G. S., Wu, Y. S., & Zhang, K. (2003). Development of discrete flow paths in unsaturated fractures at Yucca Mountain. *Journal of Contaminant Hydrology*, 62–3, 23–42. [https://doi.org/10.1016/S0169-7722\(02\)00177-8](https://doi.org/10.1016/S0169-7722(02)00177-8)
- Brantut, N., Heap, M. J., Meredith, P. G., & Baud, P. (2013). Time-dependent cracking and brittle creep in crustal rocks: A review. *Journal of Structural Geology*, 52, 17–43. <https://doi.org/10.1016/j.jsg.2013.03.007>
- Budiansky, B., Hutchinson, J. W., & Slutsky, S. (1982). Void growth and collapse in viscous solids. In H. G. Hopkins, & M. J. Sewell (Eds.), *Mechanics of solids* (pp. 13–45). Oxford: Pergamon Press.
- Cai, Z. Y., & Bercovici, D. (2013). Two-phase damage models of magma-fracturing. *Earth and Planetary Science Letters*, 368, 1–8. <https://doi.org/10.1016/j.epsl.2013.02.023>
- Carroll, M. M. (1991). A critical state plasticity theory for porous reservoir rock. In M. Massoudi, & K. R. Rajagopal (Eds.), *Recent advances in mechanics of structured continua* (pp. 1–5). New York: ASME.
- Chaboche, J. L. (2008). A review of some plasticity and viscoplasticity constitutive theories. *International Journal of Plasticity*, 24(10), 1642–1693. <https://doi.org/10.1016/j.ijplas.2008.03.009>

- Chakrabarty, J. (1987). *Theory of plasticity* (Vol. 8, p. 791). New York: McGraw-hill.
- Chang, C. D., & Zoback, M. D. (2009). Viscous creep in room-dried unconsolidated Gulf of Mexico shale (I): Experimental results. *Journal of Petroleum Science and Engineering*, 69(3–4), 239–246. <https://doi.org/10.1016/j.petrol.2009.08.018>
- Chin, L., Boade, R. R., Prevost, J. H., & Landa, G. H. (1993). Numerical simulation of shear-induced compaction in the Ekofisk reservoir. *International Journal of Rock Mechanics and Mining*, 30(7), 1193–1200.
- Connolly, J. A. D., & Podladchikov, Y. Y. (2000). Temperature-dependent viscoelastic compaction and compartmentalization in sedimentary basins. *Tectonophysics*, 324(3), 137–168.
- Connolly, J. A. D., & Podladchikov, Y. Y. (2007). Decompression weakening and channeling instability in ductile porous media: Implications for asthenospheric melt segregation. *Journal of Geophysical Research*, 112, B10205. <https://doi.org/10.1029/2005JB004213>
- Connolly, J. A. D., & Podladchikov, Y. Y. (2015). An analytical solution for solitary porosity waves: Dynamic permeability and fluidization of nonlinear viscous and viscoplastic rock. *Geofluids*, 15(1–2), 269–292. <https://doi.org/10.1111/gfl.12110>
- Coussy, O. (2004). *Poromechanics* (2nd ed.p. 298) Chichester, England; Hoboken, NJ: Wiley.
- Crook, A. J. L., Yu, J. G., Flateboe, R. E., & Kristiansen, T. G. (2008). Computational modelling of the rate dependent deformation and liquefaction of chalk, in *42nd US Rock Mechanics Symposium*, Edited, ARMA, San Francisco, USA.
- Curran, J. H., & Carroll, M. M. (1979). Shear-stress enhancement of void compaction. *Journal of Geophysical Research*, 84(Nb3), 1105–1112.
- David, C., Wong, T. F., Zhu, W. L., & Zhang, J. X. (1994). Laboratory measurement of compaction-induced permeability change in porous rocks—Implications for the generation and maintenance of pore pressure excess in the crust. *Pure and Applied Geophysics*, 143(1–3), 425–456. <https://doi.org/10.1007/BF00874337>
- Dong, J. J., Hsu, J. Y., Wu, W. J., Shimamoto, T., Hung, J. H., Yeh, E. C., et al. (2010). Stress-dependence of the permeability and porosity of sandstone and shale from TCDP Hole-A. *International Journal of Rock Mechanics and Mining*, 47(7), 1141–1157. <https://doi.org/10.1016/j.ijrmms.2010.06.019>
- Duva, J. M., & Hutchinson, J. W. (1984). Constitutive potentials for dilutely voided nonlinear materials. *Mechanics of Materials*, 3(1), 41–54.
- Eichhubl, P., Hooker, J. N., & Laubach, S. E. (2010). Pure and shear-enhanced compaction bands in Aztec Sandstone. *Journal of Structural Geology*, 32(12), 1873–1886. <https://doi.org/10.1016/j.jsg.2010.02.004>
- Fabre, G., & Pellet, F. (2006). Creep and time-dependent damage in argillaceous rocks. *International Journal of Rock Mechanics and Mining*, 43(6), 950–960. <https://doi.org/10.1016/j.ijrmms.2006.02.004>
- Fortin, J., Gueguen, Y., & Schubnel, A. (2007). Effects of pore collapse and grain crushing on ultrasonic velocities and V_p/V_s . *Journal of Geophysical Research*, 112, B08207. <https://doi.org/10.1029/2005JB004005>
- Fortin, J., Stanchits, S., Dresen, G., & Gueguen, Y. (2006). Acoustic emission and velocities associated with the formation of compaction bands in sandstone. *Journal of Geophysical Research*, 111, B10203. <https://doi.org/10.1029/2005JB003854>
- Fortin, J., Stanchits, S., Dresen, G., & Gueguen, Y. (2009). Acoustic emissions monitoring during inelastic deformation of porous sandstone: Comparison of three modes of deformation. *Pure and Applied Geophysics*, 166(5–7), 823–841. <https://doi.org/10.1007/s0024-009-0479-0>
- Fossen, H., Schultz, R. A., & Torabi, A. (2011). Conditions and implications for compaction band formation in the Navajo Sandstone, Utah. *Journal of Structural Geology*, 33(10), 1477–1490. <https://doi.org/10.1016/j.jsg.2011.08.001>
- Galin, L. A. (1946). Plane elastoplastic problem. *Prikladnaya Matematika Mekhanika*, 10(3), 367–386.
- Gerbault, M., Poliakov, A. N. B., & Daignieres, M. (1998). Prediction of faulting from the theories of elasticity and plasticity: What are the limits? *Journal of Structural Geology*, 20(2–3), 301–320. [https://doi.org/10.1016/S0191-8141\(97\)00089-8](https://doi.org/10.1016/S0191-8141(97)00089-8)
- Gerya, T. V. (2019). *Introduction to numerical geodynamic modelling* (second ed.. Ed., pages cm pp). Cambridge, United Kingdom; New York, NY: Cambridge University press.
- Gerya, T. V., & Yuen, D. A. (2003). Rayleigh-Taylor instabilities from hydration and melting propel ‘cold plumes’ at subduction zones. *Earth and Planetary Science Letters*, 212(1–2), 47–62. [https://doi.org/10.1016/S0012-821X\(03\)00265-6](https://doi.org/10.1016/S0012-821X(03)00265-6)
- Ghanbarzadeh, S., Hesse, M. A., Prodanović, M., & Gardner, J. E. (2015). Deformation-assisted fluid percolation in rock salt. *Science*, 350(6264), 1069–1072. <https://doi.org/10.1126/science.aac8747>
- Goodier, J. N. (1936). Slow viscous flow and elastic deformation. *Philosophical Magazine*, 22(149), 678–681.
- Green, R. J. (1972). Plasticity theory for porous solids. *International Journal of Mechanical Sciences*, 14(4), 215–224.
- Guéguen, Y., Dormieux, L., & Boutéca, M. (2004). Fundamentals of poromechanics. In Y. Guéguen, & M. Boutéca (Eds.), *Mechanics of fluid saturated rocks* (pp. 1–54). Amsterdam: Elsevier Academic Press.
- Gurson, A. L. (1977). Continuum theory of ductile rupture by void nucleation and growth. 1. Yield criteria and flow rules for porous ductile media. *Journal of Engineering Materials and Technology: ASME*, 99(1), 2–15.
- Hangx, S. J. T., Spiers, C. J., & Peach, C. J. (2010). Creep of simulated reservoir sands and coupled chemical-mechanical effects of CO₂ injection. *Journal of Geophysical Research*, 115, B09205. <https://doi.org/10.1029/2009jb006939>
- Heap, M. J., Brantut, N., Baud, P., & Meredith, P. G. (2015). Time-dependent compaction band formation in sandstone. *Journal of Geophysical Research: Solid Earth*, 120, 4808–4830. <https://doi.org/10.1002/2015JB012022>
- Heeres, O. M., Suiker, A. S. J., & de Borst, R. (2002). A comparison between the Perzyna viscoplastic model and the consistency viscoplastic model. *European Journal of Mechanics - A/Solids*, 21(1), 1–12. [https://doi.org/10.1016/S0997-7538\(01\)01188-3](https://doi.org/10.1016/S0997-7538(01)01188-3)
- Jordan, J. S., Hesse, M. A., & Rudge, J. F. (2018). On mass transport in porosity waves. *Earth and Planetary Science Letters*, 485, 65–78. <https://doi.org/10.1016/j.epsl.2017.12.024>
- Kachanov, L. M. (1971). *Foundations of the theory of plasticity* (Vol. 13, p. 482 p. with illus. Pp). Amsterdam: North-Holland pub. Co.
- Katz, R. F., Spiegelman, M., & Holtzman, B. (2006). The dynamics of melt and shear localization in partially molten aggregates. *Nature*, 442(7103), 676–679. <https://doi.org/10.1038/nature05039>
- Keller, T., May, D. A., & Kaus, B. J. P. (2013). Numerical modelling of magma dynamics coupled to tectonic deformation of lithosphere and crust. *Geophysical Journal International*, 195(3), 1406–1442. <https://doi.org/10.1093/gji/ggt306>
- Kohlstedt, D. L., & Holtzman, B. K. (2009). Shearing melt out of the Earth: An experimentalist’s perspective on the influence of deformation on melt extraction. *Annual Review of Earth and Planetary Sciences*, 37, 561–593. <https://doi.org/10.1146/annurev.earth.031208.100104>
- Koplik, J., & Needleman, A. (1988). Void growth and coalescence in porous plastic solids. *International Journal of Solids and Structures*, 24(8), 835–853.
- Labuz, J. F., Zeng, F. T., Makhnenco, R., & Li, Y. (2018). Brittle failure of rock: A review and general linear criterion. *Journal of Structural Geology*, 112, 7–28. <https://doi.org/10.1016/j.jsg.2018.04.007>
- Lopatnikov, S. L., & Cheng, A. H. D. (2004). Macroscopic Lagrangian formulation of poroelasticity with porosity dynamics. *Journal of the Mechanics and Physics of Solids*, 52(12), 2801–2839. <https://doi.org/10.1016/j.jmps.2004.05.005>
- Lyakhovsky, V., Zhu, W. L., & Shalev, E. (2015). Visco-poroelastic damage model for brittle-ductile failure of porous rocks. *Journal of Geophysical Research: Solid Earth*, 120, 2179–2199. <https://doi.org/10.1002/2014JB011805>

- Ma, L., & Daemen, J. J. K. (2006). An experimental study on creep of welded tuff. *International Journal of Rock Mechanics and Mining*, 43(2), 282–291. <https://doi.org/10.1016/j.ijrmms.2005.07.002>
- Makhnenko, R., & Labuz, J. (2014). Plane strain testing with passive restraint. *Rock Mechanics and Rock Engineering*, 47(6), 2021–2029. <https://doi.org/10.1007/s00603-013-0508-2>
- Makhnenko, R., & Labuz, J. F. (2015). Dilatant hardening of fluid-saturated sandstone. *Journal of Geophysical Research: Solid Earth*, 120, 909–922. <https://doi.org/10.1002/2014JB011287>
- Makhnenko, R., & Labuz, J. F. (2016). Elastic and inelastic deformation of fluid-saturated rock. *Philosophical Transactions of the Royal Society A*, 374(2078), 20150422. <https://doi.org/10.1098/rsta.2015.0422>
- Makhnenko, R., & Podladchikov, Y. Y. (2018). Experimental poroviscoelasticity of common sedimentary rocks. *Journal of Geophysical Research: Solid Earth*, 123, 7586–7603. <https://doi.org/10.1029/2018JB015685>
- Maranini, E., & Brignoli, M. (1999). Creep behaviour of a weak rock: Experimental characterization. *International Journal of Rock Mechanics and Mining*, 36(1), 127–138. [https://doi.org/10.1016/S0148-9062\(98\)00171-5](https://doi.org/10.1016/S0148-9062(98)00171-5)
- Mckenzie, D. (1984). The generation and compaction of partially molten rock. *Journal of Petrology*, 25(3), 713–765.
- Minakov, A. V., Yarushina, V. M., Faleide, J. I., Krupnova, N., Sakoulina, T., Dergunov, N., & Glebovsky, V. (2017). *Dyke emplacement and crustal structure within a continental large igneous province—Northern Barents Sea, Special Publications* (J). London: Geological Society.
- Omlin, S., Rass, L., & Podladchikov, Y. Y. (2018). Simulation of three-dimensional viscoelastic deformation coupled to porous fluid flow. *Tectonophysics*, 746, 695–701. <https://doi.org/10.1016/j.tecto.2017.08.012>
- Perzyna, P. (1966). Fundamental problems in viscoplasticity. In G. G. Chernyi, H. L. Dryden, P. Germain, L. Howarth, W. Olszak, W. Prager, et al. (Eds.), *Advances in applied mechanics* (pp. 243–377). New York and London: Academic Press. [https://doi.org/10.1016/S0065-2156\(08\)70009-7](https://doi.org/10.1016/S0065-2156(08)70009-7)
- Perzyna, P., & Drabik, A. (1989). Description of micro-damage process by porosity parameter for nonlinear viscoplasticity. *Archives of Mechanics*, 41(6), 895–908.
- Petrini, C., Gerya, T., Yarushina, V., van Dinther, Y., Connolly, J., & Madonna, C. (2020). Seismo-hydro-mechanical modelling of the seismic cycle: Methodology and implications for subduction zone seismicity. *Tectonophysics*, 791, 228504. <https://doi.org/10.1016/j.tecto.2020.228504>
- Poliakov, A. N. B., Podladchikov, Y., & Talbot, C. (1993). Initiation of salt diapirs with frictional overburdens—Numerical experiments. *Tectonophysics*, 228(3–4), 199–210. [https://doi.org/10.1016/0040-1951\(93\)90341-G](https://doi.org/10.1016/0040-1951(93)90341-G)
- Räss, L., Duretz, T., & Podladchikov, Y. Y. (2019). Resolving hydromechanical coupling in two and three dimensions: spontaneous channelling of porous fluids owing to decompression weakening. *Geophysical Journal International*, 218(3), 1591–1616. <https://doi.org/10.1093/gji/ggz239>
- Räss, L., Yarushina, V. M., Simon, N. S. C., & Podladchikov, Y. Y. (2014). Chimneys, channels, pathway flow or water conducting features –An explanation from numerical modelling and implications for CO₂ storage. *Energy Procedia*, 63, 3761–3774. <https://doi.org/10.1016/j.egypro.2014.11.405>
- Regenauer-Lieb, K., & Yuen, D. A. (2003). Modeling shear zones in geological and planetary sciences: Solid- and fluid-thermal-mechanical approaches. *Earth Science Reviews*, 63(3–4), 295–349. [https://doi.org/10.1016/S0012-8252\(03\)00038-2](https://doi.org/10.1016/S0012-8252(03)00038-2)
- Renner, J., Stockhert, B., Zerbian, A., Roller, K., & Rummel, F. (2001). An experimental study into the rheology of synthetic polycrystalline coesite aggregates. *Journal of Geophysical Research*, 106(B9), 19,411–19,429. <https://doi.org/10.1029/2001jb000431>
- Ricard, Y., & Bercovici, D. (2003). Two-phase damage theory and crustal rock failure: The theoretical ‘void’ limit, and the prediction of experimental data. *Geophysical Journal International*, 155(3), 1057–1064.
- Rice, J. R. (1992). Fault stress states, pore pressure distributions and the weakness of the San Andreas fault. In B. Evans, & T.-F. Wong (Eds.), *Fault mechanics and transport properties of rocks* (pp. 475–503). New York: Academic Press.
- Rice, J. R., & Tracey, D. M. (1969). On ductile enlargement of voids in triaxial stress fields. *Journal of the Mechanics and Physics of Solids*, 17(3), 201–217.
- Richard, G. C., Kanjilal, S., & Schmeling, H. (2012). Solitary-waves in geophysical two-phase viscous media: A semi-analytical solution. *Physics of the Earth and Planetary Interiors*, 198, 61–66. <https://doi.org/10.1016/j.pepi.2012.03.001>
- Rudge, J. F., & Bercovici, D. (2015). Melt-band instabilities with two-phase damage. *Geophysical Journal International*, 201(2), 640–651. <https://doi.org/10.1093/gji/ggv040>
- Rudnicki, J. W., & Rice, J. R. (1975). Conditions for localization of deformation in pressure-sensitive dilatant materials. *Journal of the Mechanics and Physics of Solids*, 23(6), 371–394. [https://doi.org/10.1016/0022-5096\(75\)90001-0](https://doi.org/10.1016/0022-5096(75)90001-0)
- Rybicki, E., Reinicke, A., Meier, T., Makasi, M., & Dresen, G. (2015). What controls the mechanical properties of shale rocks?—Part I: Strength and Young’s modulus. *Journal of Petroleum Science and Engineering*, 135, 702–722. <https://doi.org/10.1016/j.petrol.2015.10.028>
- Sabitova, A. I., Yarushina, V. M., Stanchits, S. A., Stukachev, V. I., & Myasnikov, A. V. (2019). Bulk viscosity measurements in creep experiments, in *81st EAGE Conference and Exhibition*, edited, London.
- Schmeling, H. (2000). Partial melting and melt segregation in a convecting mantle. In N. Bagdassarov, D. Laporte, & A. B. Thompson (Eds.), *Physics and chemistry of partially molten rocks* (pp. 141–178). Dordrecht: Kluwer Academic Publishers.
- Schmeling, H., Kruse, J. P., & Richard, G. (2012). Effective shear and bulk viscosity of partially molten rock based on elastic moduli theory of a fluid filled poroelastic medium. *Geophysical Journal International*, 190(3), 1571–1578. <https://doi.org/10.1111/j.1365-246X.2012.05596.x>
- Schofield, A. N., & Wroth, P. (1968). *Critical state soil mechanics* (Vol. 19, p. 310). New York: McGraw-hill.
- Scott, D. R., & Stevenson, D. J. (1984). Magma solitons. *Geophysical Research Letters*, 11(11), 1161–1164.
- Sevostianov, I., & Kachanov, M. (2001). On the yield condition for anisotropic porous materials. *Materials Science and Engineering a-Structural Materials Properties Microstructure and Processing*, 313(1–2), 1–15.
- Shapiro, S. A. (2003). Elastic piezosensitivity of porous and fractured rocks. *Geophysics*, 68(2), 482–486. <https://doi.org/10.1190/1.1567215>
- Skurtveit, E., Torabi, A., Gabrielsen, R. H., & Zoback, M. D. (2013). Experimental investigation of deformation mechanisms during shear-enhanced compaction in poorly lithified sandstone and sand. *Journal of Geophysical Research: Solid Earth*, 118, 4083–4100. <https://doi.org/10.1002/jgrb.50342>
- Spiegelman, M. (2003). Linear analysis of melt band formation by simple shear. *Geochemistry, Geophysics, Geosystems*, 4(9), 8615. <https://doi.org/10.1029/2002GC000499>
- Spiegelman, M., & Mckenzie, D. (1987). Simple 2-D models for melt extraction at midocean ridges and island arcs. *Earth and Planetary Science Letters*, 83(1–4), 137–152.
- Stanchits, S., Mayr, S., Shapiro, S., & Dresen, G. (2011). Fracturing of porous rock induced by fluid injection. *Tectonophysics*, 503(1–2), 129–145. <https://doi.org/10.1016/j.tecto.2010.09.022>

- Stefanov, Y. P., Chertov, M. A., Aidagulov, G. R., & Myasnikov, A. V. (2011). Dynamics of inelastic deformation of porous rocks and formation of localized compaction zones studied by numerical modeling. *Journal of the Mechanics and Physics of Solids*, 59(11), 2323–2340. <https://doi.org/10.1016/j.jmps.2011.08.002>
- Stevenson, D. J., & Scott, D. R. (1991). Mechanics of fluid-rock systems. *Annual Review of Fluid Mechanics*, 23, 305–339.
- Tsai, L. S., Hsieh, Y. M., Weng, M. C., Huang, T. H., & Jeng, F. S. (2008). Time-dependent deformation behaviors of weak sandstones. *International Journal of Rock Mechanics and Mining*, 45(2), 144–154. <https://doi.org/10.1016/j.ijrmms.2007.04.008>
- Vajdova, V., Baud, P., & Wong, T. F. (2004). Compaction, dilatancy, and failure in porous carbonate rocks. *Journal of Geophysical Research*, 109, B05204. <https://doi.org/10.1029/2003JB002508>
- Weng, M. C., Tsai, L. S., Hsieh, Y. M., & Jeng, F. S. (2010). An associated elastic-viscoplastic constitutive model for sandstone involving shear-induced volumetric deformation. *International Journal of Rock Mechanics and Mining*, 47(8), 1263–1273. <https://doi.org/10.1016/j.ijrmms.2010.08.022>
- Xiao, X. H., & Evans, B. (2003). Shear-enhanced compaction during non-linear viscous creep of porous calcite-quartz aggregates. *Earth and Planetary Science Letters*, 216(4), 725–740. [https://doi.org/10.1016/S0012-821X\(03\)00536-3](https://doi.org/10.1016/S0012-821X(03)00536-3)
- Xiao, X. H., Evans, B., & Bernabe, Y. (2006). Permeability evolution during non-linear viscous creep of calcite rocks. *Pure and Applied Geophysics*, 163(10), 2071–2102. <https://doi.org/10.1007/s00024-006-0115-1>
- Yarushina, V. M., Bercovici, D., & Oristaglio, M. L. (2013). Rock deformation models and fluid leak-off in hydraulic fracturing. *Geophysical Journal International*, 194(3), 1514–1526. <https://doi.org/10.1093/gji/ggt199>
- Yarushina, V. M., Dabrowski, M., & Podladchikov, Y. Y. (2010). An analytical benchmark with combined pressure and shear loading for elastoplastic numerical models. *Geochemistry, Geophysics, Geosystems*, 11, Q08006. <https://doi.org/10.1029/2010GC003130>
- Yarushina, V. M., & Podladchikov, Y. Y. (2007). The effect of nonhydrostaticity on elastoplastic compaction and decompression. *Izvestiya Physics of the Solid Earth*, 43(1), 67–74. <https://doi.org/10.1134/S1069351307010077>
- Yarushina, V. M., & Podladchikov, Y. Y. (2015). (De)compaction of porous viscoelastoplastic media: Model formulation. *Journal of Geophysical Research: Solid Earth*, 120, 4146–4170. <https://doi.org/10.1002/2014JB011258>
- Yarushina, V. M., Podladchikov, Y. Y., & Connolly, J. A. D. (2015). (De)compaction of porous viscoelastoplastic media: Solitary porosity waves. *Journal of Geophysical Research: Solid Earth*, 120, 4843–4862. <https://doi.org/10.1002/2014JB011260>
- Yarushina, V. M., Podladchikov, Y. Y., Minakov, A. N., & Räss, L. (2017). On the mechanisms of stress-triggered seismic events during fluid injection, in *6th Biot Conference on Poromechanics*, Edited, pp. 795–800, Paris, France, doi:<https://doi.org/10.1061/9780784480779.098>
- Yarushina, V. M., Räss, L., Simon, N. S. C., & Podladchikov, Y. Y. (2015). Shear-induced dilation and its implications for chimney flow in porous rocks, paper presented at Second EAGE Workshop on Geomechanics and Energy, Celle, Germany.
- Zhang, Y., Shao, J. F., Xu, W. Y., & Jia, Y. (2016). Time-dependent behavior of cataclastic rocks in a multi-loading triaxial creep test. *Rock Mechanics and Rock Engineering*, 49(9), 3793–3803. <https://doi.org/10.1007/s00603-016-0948-6>
- Zhang, Y., Shao, J. F., Xu, W. Y., Jia, Y., & Zhao, H. B. (2015). Creep behaviour and permeability evolution of cataclastic sandstone in triaxial rheological tests. *European Journal of Environmental and Civil Engineering*, 19(4), 496–519. <https://doi.org/10.1080/19648189.2014.960103>
- Zhu, W. L., Montesi, L. G. J., & Wong, T. F. (1997). Shear-enhanced compaction and permeability reduction: Triaxial extension tests on porous sandstone. *Mechanics of Materials*, 25(3), 199–214.